

# EDGE: The emergence of dwarf galaxy scaling relations from cosmological radiation-hydrodynamics simulations

Martin P. Rey,<sup>1,2\*</sup> Ethan Taylor,<sup>3</sup> Emily I. Gray,<sup>3</sup> Stacy Y. Kim,<sup>4</sup> Eric P. Andersson,<sup>5</sup> Andrew Pontzen,<sup>6</sup> Oscar Agertz,<sup>7</sup> Justin I. Read,<sup>3</sup> Corentin Cadiou,<sup>8,7</sup> Robert M. Yates,<sup>9</sup> Matthew D. A. Orkney,<sup>10,11</sup> Dirk Scholte,<sup>12</sup> Amélie Saintonge,<sup>13,14</sup> Joseph Breneman,<sup>15</sup> Kristen B. W. McQuinn,<sup>15,16</sup> Claudia Muni,<sup>13</sup> and Payel Das<sup>3</sup>

<sup>1</sup> *University of Bath, Department of Physics, Claverton Down, Bath, BA2 7AY, UK*

<sup>2</sup> *Sub-department of Astrophysics, University of Oxford, DWB, Keble Road, Oxford OX1 3RH, UK*

<sup>3</sup> *Department of Physics, University of Surrey, Guildford GU2 7XH, UK*

<sup>4</sup> *Carnegie Theoretical Astrophysics Center, Carnegie Observatories, 813 Santa Barbara St, Pasadena, CA 91106, USA*

<sup>5</sup> *Department of Astrophysics, American Museum of Natural History, 200 Central Park West, New York, NY 10024, USA*

<sup>6</sup> *Institute for Computational Cosmology, Department of Physics, Durham University, South Road, Durham, DH1 3LE, UK*

<sup>7</sup> *Lund Observatory, Division of Astrophysics, Department of Physics, Lund University, Box 43, SE-221 00 Lund, Sweden*

<sup>8</sup> *Institut d'Astrophysique de Paris, Sorbonne Universit'es, CNRS, UMR 7095, 98 bis bd Arago, 75014 Paris, France*

<sup>9</sup> *Centre for Astrophysics Research, University of Hertfordshire, Hatfield, AL10 9AB, UK*

<sup>10</sup> *Institut de Ciències del Cosmos (ICCUB), Universitat de Barcelona (IEEC-UB), Martí i Franquès 1, E08028 Barcelona, Spain*

<sup>11</sup> *Institut d'Estudis Espacials de Catalunya (IEEC), E-08034 Barcelona, Spain*

<sup>12</sup> *Institute for Astronomy, University of Edinburgh, Royal Observatory, Edinburgh EH9 3HJ, UK*

<sup>13</sup> *Department of Physics and Astronomy, University College London, Gower Street, London, WC1E 6BT, UK*

<sup>14</sup> *Max-Planck-Institut für Radioastronomie (MPIfR), Auf dem Hügel 69, D-53121 Bonn, Germany*

<sup>15</sup> *Department of Physics and Astronomy, Rutgers, The State University of New Jersey, 136 Frelinghuysen Rd, Piscataway, NJ 08854, USA*

<sup>16</sup> *Space Telescope Science Institute, 3700 San Martin Drive, Baltimore, MD 21218, USA*

Submitted to MNRAS

## ABSTRACT

We present a new suite of EDGE (‘Engineering Dwarfs at Galaxy formation’s Edge’) cosmological zoom simulations. The suite includes 15 radiation-hydrodynamical dwarf galaxies covering the ultra-faint to the dwarf irregular regime ( $10^4 \leq M_\star(z=0) \leq 10^8 M_\odot$ ) to enable comparisons with observed scaling relations. Each object in the suite is evolved at high resolution ( $\approx 3$  pc) and includes stellar radiation, winds and supernova feedback channels. We compare with previous EDGE simulations without radiation, finding that radiative feedback results in significantly weaker galactic outflows. This generalises our previous findings to a wide mass range, and reveals that the effect is most significant at low  $M_\star$ . Despite this difference, stellar masses stay within a factor of two of each other, and key scaling relations of dwarf galaxies (size-mass, neutral gas-stellar mass, gas-phase mass-metallicity) emerge correctly in both simulation suites. Only the stellar mass – stellar metallicity relation is strongly sensitive to the change in feedback. This highlights how obtaining statistical samples of dwarf galaxy stellar abundances with next-generation spectrographs will be key to probing and constraining the baryon cycle of dwarf galaxies.

**Key words:** methods: numerical – galaxies: dwarf – galaxies: ISM – galaxies: evolution – galaxies: structure

## 1 INTRODUCTION

Small ‘dwarf’ galaxies are sensitive probes of galaxy formation and dark matter physics. Within their shallow gravitational potential wells, energetic stellar processes (e.g. supernovae, stellar winds and radiation, collectively ‘feedback’) efficiently drive galactic outflows (see [Collins & Read 2022](#) for a review), making dwarf galaxies an ideal laboratory to study how feedback processes regulate the growth of galaxies over cosmic time (e.g. [Naab & Ostriker 2017](#) for a review). Furthermore, the existence of their low-mass dark matter haloes offer leading constraints on the ‘coldness’ of dark matter

(e.g. [Nadler et al. 2020](#)) while their internal dynamics directly probe if dark matter is self-interacting (see [Pontzen & Governato 2014](#); [Bullock & Boylan-Kolchin 2017](#); [Sales et al. 2022](#) for reviews).

The same low mass that makes dwarf galaxies sensitive to important physical processes has historically also made them challenging to observe and characterize. But the advent of wide-field, deep photometric surveys has now revealed an ever-growing number of classical and ultra-faint dwarf galaxies ([Simon 2019](#) for a review). This has in turn enabled dedicated programs to study the stellar chemistry and kinematics of these systems (e.g. [Ji et al. 2016a,b,c, 2020](#); [Longeard et al. 2018](#); [Buttry et al. 2022](#); [Simon et al. 2023](#); [Bruce et al. 2023](#); [Hansen et al. 2024](#)). Furthermore, the new generation of imaging can now be combined with upgrades in radio capabilities (e.g. MeerKAT)

\* E-mail: [mpr47@bath.ac.uk](mailto:mpr47@bath.ac.uk)

and multi-object spectroscopy (e.g. DESI). This has fundamentally changed our ability to characterize the gas contents and gas-phase metallicities of faint dwarf galaxies, pushing characterization to the very faintest end (e.g. McQuinn et al. 2021) and vastly extending statistical samples (e.g. Scholte et al. 2025).

This forward trend in observational capabilities and discoveries will continue in the next 5 years, spearheaded by experiments such as the Vera C. Rubin Observatory which is expected to provide a near-complete census of faint ( $M_V \approx -6$ ) dwarf galaxies within 5 Mpc around the Milky Way (Mutlu-Pakdil et al. 2021) and the Nancy Roman Space Telescope. These new photometric datasets will be complemented by forthcoming spectroscopic information, with for example the 4MOST-Dwarf survey expected to obtain chemical abundances for  $> 50,000$  dwarf galaxy stars (Skúladóttir et al. 2023).

Interpreting these new datasets requires us to develop detailed models of dwarf galaxy formation that can match the data's new statistical power while retaining enough physical fidelity to make robust predictions. This is a challenging task. The small sizes of dwarf galaxies ( $\approx 100$  pc) require high ( $\approx 10$  pc) numerical resolution to resolve their gas reservoirs and star-forming regions over cosmic time. But, at the same time, modelling the full cosmological history of a dwarf galaxy is also essential, as each specific formation scenario plays a key role in setting the  $z = 0$  properties and observables (e.g. Benítez-Llambay et al. 2015; Benítez-Llambay & Fumagalli 2021; Fitts et al. 2017; Rey et al. 2019b, 2020; Wright et al. 2019; Katz et al. 2020; Tarumi et al. 2021; Herzog et al. 2023). Simulating many objects, in a cosmological context, and with a high resolution places conflicting demands on the available computing power.

Nonetheless, the field has made great progress in addressing these challenges in recent years. Improvements in code efficiency and computational power now allow zoomed cosmological simulations of isolated faint dwarf galaxies with  $\approx$  pc resolution over the full Hubble time (e.g. Wheeler et al. 2019; Agertz et al. 2020; Gutcke et al. 2022). These gains go beyond an incremental improvement in resolution, as they allow us to resolve explicitly the cooling radius of supernovae (SNe) explosions, in turn enabling a robust modelling of the emerging momentum and its coupling to the gas (e.g. Kimm et al. 2015; Kim & Ostriker 2015; Martizzi et al. 2015; Ohlin et al. 2019).

In parallel, model improvements are significantly increasing physical fidelity. For example, radiation-hydrodynamics simulations can now account for stellar radiative heating over the cosmological history of a dwarf galaxy (Ageretz et al. 2020). Unlike previous subgrid implementation that were attempted to capture radiative effects locally (e.g. Agertz et al. 2013; Hopkins et al. 2018), explicit radiative transfer gives a physical account of how photons ionize, heat and inject momentum in the gas both locally, and non-locally across the ISM and CGM. Beyond radiative transfer, cosmological simulations of dwarf galaxies have also made strides to explicitly sample the initial mass function with individual stars (e.g. Gutcke et al. 2022; Andersson et al. 2025), unlocking direct comparisons with resolved-star observations of dwarf galaxies in the Local Volume. And high-resolution cosmological simulations have also started to incorporate detailed models of cosmic ray (e.g. Martín-Alvarez et al. 2023) and black hole feedback (e.g. Koudmani et al. 2021, 2022; Arjona-Galvez et al. 2024), starting to quantify the importance of these processes at the faint end of galaxy formation at  $z = 0$ .

Furthermore, lessons learned from these detailed numerical simulations directly inform the development of more realistic semi-analytical and semi-empirical models of dwarf galaxy formation (e.g. Benítez-Llambay & Frenk 2020; Wang et al. 2021; Kravtsov & Manwadkar 2022; O'Leary et al. 2023; Kim et al. 2024; Monzon et al. 2024). The statistical power of these models will be invaluable

to interpret the populations of dwarf galaxies from next-generation surveys.

The EDGE collaboration has been a key contributor to these advances. At the core of our approach is the undertaking of suites of highly-detailed, high-resolution cosmological simulations (e.g. Agertz et al. 2020; Rey et al. 2020; Prgomet et al. 2022; Andersson et al. 2025). These simulations are then leveraged to pinpoint the key factors shaping dwarf galaxy observables (Rey et al. 2019b, 2022, 2024b; Goater et al. 2024; Gray et al. 2024), and dark matter properties (Orkney et al. 2021, 2022, 2023). Learnings from these simulations are then encapsulated into a semi-analytical model to enable the modelling of statistical populations (Kim et al. 2024).

In this paper, we present the new generation of EDGE cosmological zoomed simulations that will be the cornerstone of our future interpretation efforts. This new suite extends the state of the art in multiple ways. First, in physical fidelity. We maintain the characteristic high resolution of the original EDGE simulations ( $\Delta x \approx 3$  pc;  $m_{\text{DM}} \approx 950 M_{\odot}$ ) to resolve individual SNe explosions, and combine it with a systematic use of radiative transfer for an explicit account of radiative feedback from stars. This improves the physical realism of the interstellar medium (ISM) over many more objects than the single dwarf galaxy presented in Agertz et al. (2020).

Second, we extend the scale of the simulation suite. We simulate  $> 15$  different dwarf galaxies from ultra-faint dwarf galaxies ( $M_{200} \approx 10^9 M_{\odot}$ ;  $M_{\star} \approx 10^4 M_{\odot}$  at  $z = 0$ ) to dwarf irregulars ( $M_{200} \approx 10^{10} M_{\odot}$ ;  $M_{\star} \approx 10^7 M_{\odot}$ ). All simulations share the same numerical resolution and feedback physics. Bridging to higher-mass objects without compromising on the physical fidelity opens new regimes of comparisons with observational data, as well as providing a larger range of data points to calibrate future semi-analytical models.

This combination of scale and fidelity is unique. Furthermore, the ability to compare between two fundamentally different feedback models (without and with photo-ionization feedback in EDGE1 and EDGE2, respectively) also allows for a new understanding of the theoretical uncertainties in our results. We describe the EDGE2 model and its updates in Section 2 and show how it affects the ISM and outflows of dwarf galaxies in Section 3. Section 4 shows how dwarf galaxy scaling relations naturally emerge from EDGE modelling and their robustness to a large change in sub-grid physics modelling. Section 5 discusses the new numerical challenges associated with explicitly modelling stellar radiation, and we conclude in Section 6.

## 2 EDGE2 NUMERICAL SETUP

In this section, we describe the EDGE2 numerical methods and the suite of zoomed cosmological simulations. We briefly summarize the main differences between EDGE1 and EDGE2 in the bullet points below, and refer the reader to Rey et al. (2020) for a more in-depth description of the EDGE1 model.

- EDGE2 uses non-equilibrium primordial and molecular chemistry via the implementation of Rosdahl et al. (2013); Nickerson et al. (2018), as opposed to EDGE1's equilibrium cooling from Courty & Alimi (2004).
- EDGE2 accounts for stellar photo-ionization and photo-heating using radiative transfer following the setup described in Agertz et al. (2020).
- EDGE2 updates the feedback budget to be normalized to a Kroupa (2001) initial mass function (IMF) integrated between 0.1 and  $100 M_{\odot}$  to be consistent with spectral energy distribution libraries. EDGE1 used a Chabrier (2003) IMF integrated between 0.5 and  $100 M_{\odot}$ .

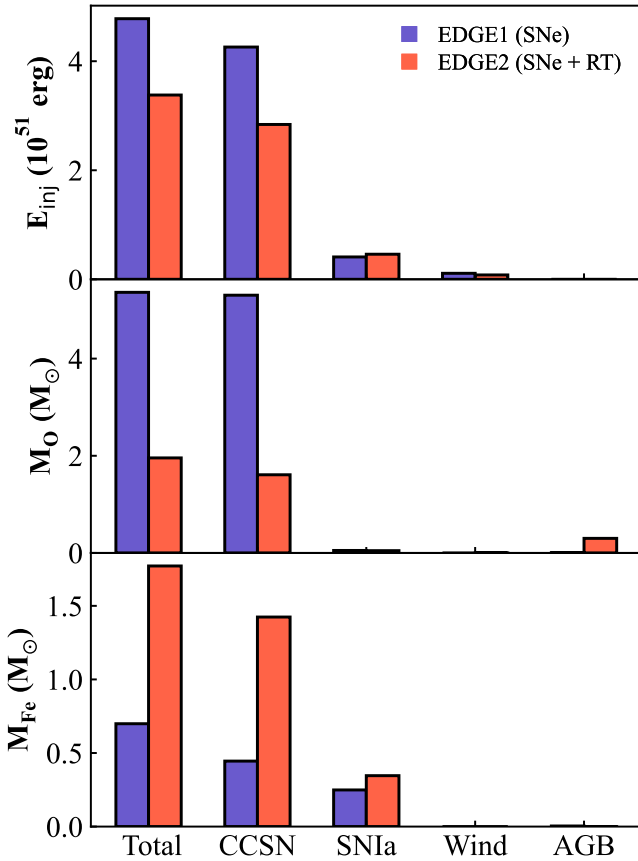


**Figure 1.** Energy (top), total oxygen (middle) and iron (bottom) injected by a  $300 M_{\odot}$  stellar particle over its lifetime in the EDGE1 and EDGE2 models. The total is the sum of each individual subcomponent and does not include the radiation budget to enable one-to-one comparison between EDGE2 and EDGE1. Due to the change in IMF, yields and SNeIa modelling, EDGE2 injects  $\approx 50\%$  less CCSN energy, half the oxygen, and twice the iron per stellar population.

- EDGE2 tracks the enrichment of eight individual elements (C, N, O, Mg, Al, Si, Fe and Eu) using the NuGRID yields for core-collapse supernovae (CCSNe; Pignatari et al. 2016; Ritter et al. 2018). EDGE1 tracked only O and Fe and used the Woosley & Heger (2007) CCSNe yields for EDGE1.
- EDGE2 updates the Type-Ia supernova (SNeIa) model to use a delay-time distribution from Maoz et al. (2012) and yields from Seitzzahl et al. (2013). EDGE1 used the binary mass function from Raiteri et al. (1996) and yields originally from Thielemann et al. (1986).
- EDGE2 updates the UV background (UVB) from a modified Haardt & Madau (1996) to the Faucher-Giguère (2020) photo-ionization and photo-heating rates.
- EDGE2 uses a new high-cadence infrastructure to allow the dynamical tracking of gas and stars on short timescales with tracer particles (Cadiou et al. 2019).
- EDGE2 adds five new objects at higher masses ( $M_{200} \approx 10^{10} M_{\odot}$ ) to the original suite of initial conditions to grow our sample size (Muni et al. 2025). Table A1 in Appendix A provides all the properties of each object in the EDGE1 and EDGE2 models.

Figure 1 summarizes how these changes affect the energy injection and metal production budget integrated over 14 billion years in a  $300 M_{\odot}$ ,  $0.01 Z_{\odot}$  stellar population. We describe these changes further in the next sections.

## 2.1 Initial conditions and resolution

All of our simulated galaxies are evolved to  $z = 0$  from cosmological zoomed initial conditions constructed with the GENETIC software (Stopyra et al. 2021a). All initial conditions use a flat  $\Lambda$ CDM transfer function generated with CAMB (Lewis et al. 2000). Original EDGE1 initial conditions assume a Planck Collaboration et al. (2014) cosmology with parameters  $\Omega_m = 0.3086$ ,  $\Omega_{\Lambda} = 0.6914$ ,  $h = 0.6777$ ,  $\sigma_8 = 0.8288$ ,  $n_s = 0.9611$ . The new initial conditions we introduce below use a Planck Collaboration et al. (2020) cosmology with parameters  $\Omega_m = 0.3158$ ,  $\Omega_{\Lambda} = 0.6842$ ,  $h = 0.6732$ ,  $\sigma_8 = 0.8117$ ,  $n_s = 0.9660$ . These cosmologies are compatible within 68% confidence intervals and do not lead to major differences. Initial conditions are evolved analytically using first-order perturbation theory (Zel’dovich 1970) until  $z = 99$ , at which point numerical integration starts.

To build the original EDGE1 zoomed regions, we first simulate a random cosmological volume (50 Mpc at  $512^3$  resolution) only accounting for gravity and dark matter. We then open a cubic zoomed region of 11.5 Mpc (resolution equivalent to  $2048^3$ ,  $m_{\text{DM}} = 3.8 \times 10^6 M_{\odot}$ ) centred on the largest void in the simulation. Having resimulated this first zoom level, we identify haloes within the  $z = 0$  void using the HOP halo finder (as in Eisenstein & Hut 1998) and keep only isolated central haloes with no neighbours more massive than them within  $5r_{200}$ . Here,  $r_{200}$  is the radius encompassing 200 times the critical density of the Universe. We select six dark matter haloes spanning a wide window in present-day halo mass ( $M_{200} = 1.5 \times 10^9$  to  $7 \times 10^9 M_{\odot}$ , where  $M_{200}$  is the mass enclosed in a sphere of radius  $r_{200}$ ), track them back to the initial conditions again, and generate initial conditions at our final zoomed resolution ( $m_{\text{DM}} = 940 M_{\odot}$ , equivalent to  $16384^3$ ).

New initial conditions presented in this paper follow the same procedure as previously followed with small operational differences (see also Muni et al. 2025). The original volume is 100 Mpc, first simulated using  $256^3$  particles. We centre on the biggest void identified by running a ‘paired’ simulation (see Stopyra et al. 2021b) and select a  $\approx 11.5$  Mpc cubic subvolume in which the resolution reaches  $m_{\text{DM}} = 3.9 \times 10^6 M_{\odot}$ . We select three haloes with present-day halo masses from  $M_{200} = 7 \times 10^9$  to  $1 \times 10^{10} M_{\odot}$  and increase the dark matter resolution in their Lagrangian region to  $m_{\text{DM}} = 953 M_{\odot}$ . Resolution between the original and updated initial conditions match to  $\approx 1\%$ , with slight shift arising from the slight differences in cosmological parameters.

We also use the ‘genetic modification’ approach to introduce controlled changes in cosmological initial conditions (see Roth et al. 2016; Rey & Pontzen 2018; Stopyra et al. 2021a; Cadiou et al. 2021 for more information about the method and the range of possible modifications). Using this approach, all initial conditions are genetically-modified to ensure that the Lagrangian region of our dwarf galaxies is (almost) at rest with respect to the cosmological box (Pontzen et al. 2021). This modification minimizes the streaming of the dwarf galaxy through the simulated volume, mitigating advection errors during integration without affecting its mass growth and local environment.

Furthermore, four of our haloes have genetically-modified initial conditions that craft a targeted change to their mass growth history. One low-mass halo (‘Halo 1459’) is engineered to form systematically earlier and later, at fixed halo mass today (see Rey et al. 2019b). Two intermediate mass haloes (‘Halo 624’, ‘Halo 600’) are modified to respectively be more massive in halo mass overall and to form later at fixed  $z = 0$  halo mass (see Rey et al. 2020). Lastly, a high-mass halo (‘Halo 383’) is modified to form earlier and later at fixed

halo mass today (see [Gray et al. 2024](#)). Thanks to the nature of the genetic modification algorithm, all other untargeted aspects of each formation scenario is maximally reproduced (e.g. the large-scale environment and cosmic web topology; see e.g. [Pontzen et al. 2017](#); [Rey et al. 2019a](#) for visuals). All haloes labelled ‘GM’ in [Table A1](#) have had their mass accretion histories genetically modified. Future work will perform controlled modifications to additional haloes in the EDGE2 suite.

## 2.2 Hydrodynamics, radiative transfer and refinement

We follow the evolution of dark matter, stars, gas and radiation using the adaptative mesh refinement hydrodynamics code RAMSES-RT ([Teyssier 2002](#); [Rosdahl et al. 2013](#)). The dynamics of collisionless particles (dark matter and stars) are computed using a multiscale particle-mesh solver estimating densities through a cloud-in-cell approximation ([Guillet & Teyssier 2011](#)). Fluid dynamics are computed using an HLLC Riemann solver ([Toro et al. 1994](#)) with the fluid equations closed by assuming an ideal gas equation of state with adiabatic index  $\gamma = 5/3$ .

A key addition to this suite is the explicit treatment of the local sources of radiation. We solve the dynamics of the radiation field using the M1 method ([Rosdahl et al. 2013](#); [Rosdahl & Teyssier 2015](#)) discretizing the light spectrum in six energy bins from the infrared to the UV (same as in [Agertz et al. 2020](#), table 1). Our energy bins are chosen to track radiation that (i) exerts radiation pressure through dust multi-scattering (from 0.1 to 1 eV), (ii) exerts direct radiation pressure (from 1 to 12 eV), (iii) dissociates H<sub>2</sub> (from 12 to 13.6 eV), (iv) ionizes H I (13.6 to 24.59 eV), (v) ionizes He I (24.59 to 54.42 eV), and (vi) ionizes He II (> 54.42 eV). We update the average energies and cross-sections in each band every 10 coarse time-steps by computing the luminosity-weighted average over the spectra of all stellar populations in the simulation volume (see [Rosdahl et al. 2013](#)). Furthermore, to mitigate computational costs, local radiation around stellar sources is propagated at a reduced speed of light ( $c_{\text{reduced}} = c/100$ ; see discussions in e.g. [Gnedin & Abel 2001](#); [Rosdahl et al. 2013](#)). A time-varying, but spatially uniform, UVB also permeates the simulation box after reionization (see [Section 2.3](#)). This source is not propagated but contributes to photo-ionization and photo-heating rates.

We use the adaptative nature of RAMSES-RT to focus computational power in the dense centre of our dwarf galaxies during integration. We split cells when they contain 8 dark matter particles, and when their baryonic mass (stars and gas) exceeds  $8 m_{\text{bar}}$ , where  $m_{\text{bar}} \approx 150 M_{\odot}$ . Refinement is allowed down to a maximum resolution of  $\Delta x \approx 3$  physical pc. This maximum resolution is achieved throughout the dwarf galaxy’s ISM and rapidly degrades as densities decrease (see e.g. [Pontzen et al. 2021](#), fig. 3). We maintain an approximately constant resolution in physical units by releasing additional new levels every two-folding of the scale factor ([Snaith et al. 2018](#)). Refinement is only allowed inside the zoomed region.

## 2.3 Cooling and thermochemistry

Compared to the original EDGE simulations that assumed equilibrium chemistry and cooling, the new simulations of this paper now follow the non-equilibrium thermo-chemistry of the primordial plasma fully coupled to radiative transfer.

We track the individual ionization fractions of H I, H II, He I, He II, He III and H<sub>2</sub>. The mass fractions and cooling contributions from atomic species are computed using the semi-implicit solver

described in [Rosdahl et al. \(2013\)](#), accounting for photoionisation, collisional ionisation and excitation, bremsstrahlung, Compton cooling and heating from the cosmic microwave background, and dielectronic recombination. We assume that ionizing radiation from free-bound ground state recombination radiation is absorbed locally (the on-the-spot approximation; see e.g. [Nebrin 2023](#)). We follow the formation, advection and destruction of H<sub>2</sub> and its contribution to the cooling rate following the model described in [Nickerson et al. \(2018\)](#). This model accounts for gas-phase, dust-phase and collisional H<sub>2</sub> formation, destruction through photodissociation, photoionization, cosmic ray ionization, and collisions, and cooling and heating coupled to the local radiation flux.

Metal cooling uses tabulated cooling rates scaled by metallicity. Below  $10^4$  K, we use the [Rosen & Bregman \(1995\)](#) fine structure cooling rates, while above  $10^4$  K, we use CLOUDY ([Ferland et al. 2017](#)) tables assuming our updated UVB ([Faucher-Giguère 2020](#)). These rates are scaled by the total metallicity defined as  $Z = (2.09 Y_{\text{O}} + 1.06 Y_{\text{Fe}})/Z_{\odot}$ , where  $Z_{\odot} = 0.02$ . The numerical coefficients are derived from assuming a solar mixture from [Asplund et al. \(2009\)](#) and  $Y_{\text{O}}$  and  $Y_{\text{Fe}}$  are the mass fractions of oxygen and iron in the gas cell (see also [Kim et al. 2014](#)).

Ionization and heating from the UVB permeates the whole volume in an optically-thin approximation, with high density regions allowed to self-shield from this background. We exponentially damp the UVB photo-ionization and photo-heating rates according to  $\exp(-n_{\text{H}}/10^{-2} \text{ cm}^{-3})$  to approximate self-shielding above  $n_{\text{H}} \approx 10^{-2} \text{ cm}^{-3}$  ([Aubert & Teyssier 2010](#); [Rosdahl & Blaizot 2012](#)). Local self-shielding from stellar radiation is treated self-consistently by solving of the coupled equations of radiative transfer and thermochemistry. Optically thin UVBs can overheat the early intergalactic medium ([Oñorbe et al. 2017](#)), so we also exponentially damp the UVB as a function of redshift by  $\exp(z_{\text{reion}} - z)$ . This ensures a continuous ramp up of photo-ionizing and photo-heating rates, rather than the instantaneous switch-on commonly used in UVB tables (e.g. [Faucher-Giguère 2020](#)). With our choice of  $z_{\text{reion}}$ , the UVB heating and ionizing rates are at full strength at  $z = 6$  (see [Rey et al. 2020](#)).

## 2.4 Star formation

The star formation modelling remains unchanged compared to [Agertz et al. \(2020\)](#). We model star formation following a Kennicutt-Schmidt law ([Schmidt 1959](#); [Kennicutt 1998](#)):

$$\dot{\rho}_{*} = \epsilon_{\text{ff}} \frac{\rho_{\text{g}}}{t_{\text{ff}}} \text{ for gas cells with } \rho_{\text{g}} > \rho_{*} \text{ and } T_{\text{g}} < T_{*}, \quad (1)$$

where  $\dot{\rho}_{*}$  is the instantaneous star formation rate in a gas cell,  $\epsilon_{\text{ff}}$  is the star formation efficiency per free-fall time,  $\rho_{\text{g}}$  and  $T_{\text{g}}$  are the gas cell density and temperature,  $t_{\text{ff}} = \sqrt{3\pi/32G\rho}$  is the local free-fall time.  $\rho_{*} = 300 m_{\text{p}} \text{ cm}^{-3}$  and  $T_{*} = 1000$  K are imposed thresholds that gas must satisfy to qualify for star formation, and we assume  $\epsilon_{\text{ff}} = 10\%$  throughout.  $T_{*}$  is higher than in EDGE1 (100 K) to compensate for the additional heating from radiative feedback – [Section 5.1.4](#) explores the impact of this parameter in more detail.

For every gas cell satisfying our threshold conditions, we sample Equation (1) stochastically with a Poisson process so that the expectation of the local SFR equals  $\dot{\rho}_{*}$  ([Rasera & Teyssier 2006](#)). Stellar particles have initial masses of  $300 M_{\odot}$  and assume a [Kroupa \(2001\)](#) initial mass function (IMF). This mass is enough to appropriately sample massive stars and their feedback in an IMF (see e.g. [Smith 2021](#)) which is key for radiative feedback which is still modelled as



an IMF-averaged process (as opposed to SN feedback for which SNe are individually sampled).

## 2.5 Stellar feedback

A key aspect of the EDGE model is the detailed account of feedback from massive stars. We account for CCSNe, SNeIa, fast winds from massive stars, slow winds from asymptotic giant branch (AGB) stars, and now radiative feedback.

Our model tracks the main-sequence lifetime of different progenitors within a stellar particle (Agertz et al. 2011), ensuring that stars of different masses inject their feedback on their relevant main-sequence timescale. We model SN explosions as discrete events, computing at each simulation time-step the number of stars exiting the main sequence to turn into CCSNe (equations 6 in Agertz et al. 2013). This IMF-averaged number is then randomly sampled through a Poisson process to obtain a discrete number of explosions (Agertz et al. 2020). To maintain consistency with the IMF used for radiative feedback, we normalize this number to the Kroupa (2001) IMF integrated between 0.1 and  $100 M_{\odot}$ . This differs from EDGE1 which used a Chabrier (2003) IMF integrated between 0.5 and  $100 M_{\odot}$ , leading to a  $\approx 40\%$  decrease in the number of CCSNe per stellar population (Figure 1, top)

Furthermore, to match the explodability assumptions made by our new chemical enrichment model (Section 2.6), we now assume that massive stars between 8 and  $30 M_{\odot}$  explode as CCSNe, while stars above directly collapse into black holes without releasing energy. Previous EDGE1 modelling assumed that all stars between  $8 M_{\odot}$  and  $40 M_{\odot}$  exploded. When convolved with the IMF, this further reduces the energy budget of CCSNe by  $\approx 10$  per cent.

Furthermore, SNeIa now follow a delay time distribution according to Agertz et al. (2021). We assume that SNeIa start when their parent stellar particle has an age of 38.4 Myr (the main-sequence lifetime of  $8 M_{\odot}$  star to form the first non-exploding degenerate progenitor) and explode with a rate that initially peaks at  $2.6 \times 10^{-13} M_{\odot}^{-1}$  and decays as  $t^{-1.12}$  following the empirical determination of Maoz et al. (2012) for field galaxies. As for CCSNe, SNeIa are individually sampled from this rate using a Poisson process. In EDGE1, we instead modelled the SNeIa rate by integrating over the IMF of secondary, binary companions between 1 and  $8 M_{\odot}$  (Raiteri et al. 1996; see Agertz et al. 2013 for a detailed description). This modernization leads to a higher number of SNeIa per stellar population (Figure 1, top), which balances the 40% decrease induced by the change in IMF normalization.

For both SN types, we directly inject thermal energy ( $E_{\text{SN}} = 10^{51}$  erg constant at all times) when the cooling radius of the individual SN event is resolved by 6 resolution elements. This allows us to self-consistently follow the build-up of momentum through the Sedov-Taylor phase by solving the hydrodynamics equations rather than relying on a subgrid implementation. When the cooling radius is unresolved, we switch to a momentum injection (see also Kim & Ostriker 2015 for a similar implementation). Appendix B shows that  $> 90\%$  of CCSNe events and  $> 60\%$  of SNeIa events are resolved by more than  $6^3$  ( $> 200$ ) resolution elements, ensuring that we greatly reduce uncertainties associated to the subgrid modelling of SN feedback in an unresolved ISM.

We also account for wind feedback from massive O and B stars ( $m \geq 8 M_{\odot}$ ) during their main sequence, and from stars of masses  $0.5 - 8.0 M_{\odot}$  when they reach their AGB phase. OB winds return mass and momentum to the ISM according to the metallicity-dependent budget described in Agertz et al. (2013). AGB winds

continuously release mass and metals over the lifetime of a stellar particle following their IMF-averaged mass-loss (eq. 17 in Agertz et al. 2013). No changes are made to these models between EDGE1 and EDGE2 and at our characteristic low metallicities, these wind models contribute little to the feedback energy budget (Figure 1).

In addition to these changes to the SN budget between EDGE1 and EDGE2, a large change in stellar feedback comes from the addition of radiative feedback in EDGE2. In this case, each stellar particle injects radiation according to its age and metallicity following a Bruzual & Charlot (2003) spectral energy distribution (SED). This SED is a ‘soft’ choice for low-metallicity stellar populations, and we explore in Section 5.1.3 the impact of a harder SED accounting for binary stars (Stanway et al. 2016).

## 2.6 Metal enrichment

Another novelty in this suite is the tracking of new chemical elements. In addition to O and Fe tracked by the previous model (Agertz et al. 2013), we now account for the production and advection of C, N, Mg, Al, Si, and Eu. These elements were chosen to sample main  $\alpha$  elements commonly observed in stars within dwarf galaxies, as well as the r-process element Eu.

As with previous EDGE simulations, we do not model the formation, feedback and metal enrichment from primordial metal-free stars. Instead, we initialize all simulations with a floor in oxygen metallicity of  $Z_{\text{O}} = 10^{-3} Z_{\odot}$  as an approximation for primordial metal enrichment (e.g. Greif et al. 2010; Jaacks et al. 2018; Visbal et al. 2020; Brauer et al. 2025). All other elements have vanishing mass fractions initially. Lowering this floor by an order of magnitude leaves the stellar mass and metallicities of our dwarfs unchanged (Agertz et al. 2020).

Once star formation starts, winds from O and B stars, winds from AGB stars, CCSNe, and SNeIa all inject chemical elements on the same timescale as their feedback (Section 2.5). Once injected, each element is advected passively with the gas.

Yields for CCSNe, OB winds and AGB winds are interpolated from the tables provided by NuGRID (Pignatari et al. 2016; Ritter et al. 2018). Discrete injection events from CCSNe are interpolated across the table in progenitor mass and metallicity. Discrete SNeIa inject chemical elements according to Seitenzahl et al. (2013) assuming a (constant) solar metallicity (metallicity-dependence of these yields is weak). For AGB winds, we compute the IMF-averaged number of AGB stars in a given timestep (Agertz et al. 2013) and inject the corresponding yields from NuGRID for each element. OB winds follow the same procedure, but instead inject according to a time-dependent fitting function that was calibrated in Agertz et al. (2013).

Combined, these updates have a significant impact on the metal production budget per stellar population. Figure 1 shows that oxygen production is roughly halved in EDGE2 (middle panel), primarily driven by a strong decrease in CCSNe yield. Part of this decrease is due to the change in IMF normalization reducing overall CCSNe numbers by  $\approx 40\%$ , but is strongly driven by the change in yield tables. EDGE1 tables (Woosley & Heger 2007) had an exponential scaling of oxygen production with progenitor mass (see e.g. Kim & Ostriker 2015, eq. 5) with high-mass stars producing copious amounts of metals. This was known to significantly over-produce oxygen and alpha elements compared to Milky Way observations (e.g. Agertz et al. 2021). The scaling with progenitor mass is much weaker in the NuGRID tables. Importantly, iron production is increased by a factor  $\approx 2.5$  in EDGE2 (bottom panel), again largely driven by the change in CCSN yield table. This reflects the recent trends in yield computations with newer models all producing sig-

nificantly more iron than previous iterations (e.g. [Limongi & Chieffi 2018](#)).

Finally, for r-process production of Eu, we include an effective model for neutron-star mergers (NSNS) inspired by [Naiman et al. \(2018\)](#). We assume a constant relative fraction  $4.6 \times 10^{-2}$  between NSNS and SNeIa consistent with the NSNS rates observed in the local Universe ([LIGO and Virgo Scientific Collaboration et al. 2017](#)). NSNS events are sampled discretely using the same mechanism as SNeIa with each NSNS injecting a europium yield of  $10^{-5} M_{\odot}$  ([Côté et al. 2018](#)) but no other elements. NSNS events do not inject energy, mass or momentum.

## 2.7 High-cadence outputs

The Eulerian nature of our code prevents us from efficiently tracking the Lagrangian history of gas flows. This is particularly problematic in dwarf galaxies where dynamical times and cooling times in the centre are much shorter than the cadence at which we can save simulation outputs (see e.g. [Rey et al. 2022, 2024b](#) for examples of these limitations).

To remedy to this, EDGE2 uses a Monte-Carlo particle tracer algorithm ([Cadiou et al. 2019](#)). Tracers are designed to statistically track gas flows and exchange mass with stellar tracers to track the full baryon cycle of gas as it is accreted and recycled through star formation. Tracer dynamics is solved using the same physical solvers as the rest of the simulation, but they do not source or contribute towards hydrodynamical, gravity or radiative forces. We spawn five tracers per high-resolution gas cell, leading to a tracer mass of  $223 M_{\odot}$  comparable to the stellar particle mass. Our smallest dwarf galaxies have  $\approx 2$  million tracers, while our most massive objects can have up to 20 million tracers.

The position and velocity of tracers is stored on disc every 4.5 Myr (compared to every 100 Myr for full simulation output), along with the density, pressure and gravitational potential of the gas at the location of the tracer. Additionally, the same information with the same cadence is dumped for a selection of 10,000 dark matter particles, selected randomly from the main progenitor of the dwarf at  $z=2$ .

## 2.8 Data processing and analysis

We process each EDGE2 simulation with the ADAPTAHOP halo and subhalo finder ([Aubert et al. 2004; Tweed et al. 2009](#)) retaining dark matter structures with more than 100 particles. EDGE1 simulations were processed with the HOP halo finder ([Eisenstein & Hut 1998](#)). We match haloes and subhaloes between simulation snapshots to build merger trees using the PYNBODY ([Pontzen et al. 2013](#)) and TANGOS ([Pontzen & Tremmel 2018](#)) libraries. Halo centres are identified using the shrinking-sphere algorithm ([Power et al. 2003](#)).

## 3 THE IMPACT OF RADIATIVE FEEDBACK ON DWARF GALAXIES

### 3.1 The stellar mass-halo mass relation

Figure 2 shows how the integrated stellar masses,  $M_{\star}$ , respond to the change from the original EDGE1 (blue circles) to the updated EDGE2 (red diamonds) model.  $M_{\star}$  is computed by summing all stellar particles within  $r_{200}$  and lines connect dwarf galaxies sharing the same cosmological initial conditions and formation scenarios (see legend for individual names).

Comparing our results with empirical determinations of the

$M_{\star} - M_{200}$  relation from observed dwarf galaxies (left and middle panel) shows that EDGE dwarf galaxies are within observational uncertainties. In both the EDGE1 and EDGE2 models, low-mass dwarf galaxies ( $M_{\star} \approx 10^4 - 10^6 M_{\odot}$ ;  $M_{200} \approx 10^9 M_{\odot}$ ) scatter around the median inferred from Milky Way satellites (blue line showing the peak halo mass from [Nadler et al. 2020](#)) and span the breadth of the 16-84 confidence interval at fixed  $M_{200}$  (blue contours). In our suite, this scattering around the median is largely driven by our systematic exploration of different formation histories at fixed halo mass ([Rey et al. 2019b; Gray et al. 2024](#)).

An agreement between Milky-Way satellites and simulated field dwarfs might appear surprising at first. But in the low mass regime, the shutdown of gas accretion in the smallest haloes due to cosmic reionization (‘reionization feedback’) is the dominant mechanism regulating the stellar mass and gas content (e.g. [Efstathiou 1992; Gnedin 2000; Hoeft et al. 2006; Okamoto et al. 2008; Noh & McQuinn 2014; Benitez-Llambay & Frenk 2020](#)). Furthermore, few faint and ultra-faint observed dwarf galaxies have orbital parameters that lead to strong tidal interactions with the Milky Way ([Simon 2018; McConnachie & Venn 2020; McConnachie et al. 2021](#)). As a result, the faint-end of the  $M_{\star} - M_{200}$  relation is likely to be shaped by their pre-reionization ( $z \geq 6$ ) evolution, rather than limited by the specific environment of our Galaxy.

As dwarf galaxies grow in mass, ( $M_{\star} \geq 10^6 M_{\odot}$ ;  $M_{200} \geq 5 \times 10^9 M_{\odot}$ ), reionization feedback becomes less dominant. This enables field dwarf galaxies to accrete late-time gas and enable dark matter halo mass measurements through rotation curves ([Read et al. 2017](#); grey points in left-hand panel). At high  $M_{200}$  all the way to  $M_{200} \approx 10^{10} M_{\odot}$ , our simulated dwarf galaxies closely match the individual measurements of field, gas-rich dwarf irregulars. But, importantly, the two lowest mass objects in the [Read et al. \(2017\)](#) sample lack a simulated counterpart. Rather than a failure of the model, this more likely reflect the rarity of finding such low-mass, gas-rich galaxies on which to perform rotation curve measurements. At halo masses  $M_{200} \approx 2 \times 10^9 M_{\odot}$ , only very specific formation histories that form especially late will allow gas accretion and star formation ([Benitez-Llambay & Fumagalli 2021](#)). Such objects are not present either in the EDGE1 and EDGE2 suites, but calibrating a semi-analytical on EDGE1 results to create a large population naturally recovers them ([Kim et al. 2024](#)).

On average,  $M_{\star}$  in EDGE1 and EDGE2 differ by 34 per cent across the suite, and are within a factor of two of each other for all galaxies except for three specific formation histories that we discuss further below. The magnitude of these shifts is encouragingly tight given the large changes in cooling and heating physics between models. To emphasize that such shifts are well within theoretical uncertainties, the right-panel of Figure 2 shows a compilation of simulated field dwarf galaxies ([Benitez-Llambay & Fumagalli 2021; Herzog et al. 2023](#), plusses, ‘Swift’; [Revaz & Jablonka 2018](#), crosses, ‘Gear’; [Wang et al. 2015; Tollet et al. 2016](#), dots, ‘Nihao’; [Fitts et al. \(2017\); Wheeler et al. \(2019\)](#), stars, ‘FIRE-2’; [Munshi et al. \(2019, 2021\)](#), pentagons, ‘Changa’). At given  $M_{200}$ , predictions from different simulation groups can differ by over an order of magnitude in  $M_{\star}$  (e.g. pentagons against stars around  $M_{200} \approx 10^{10} M_{\odot}$ ), highlighting the small-in-comparison shifts between EDGE1 and EDGE2.

Before turning to comparing our dwarf galaxies to observations (Section 4), we highlight several trends in Figure 2 that will help us establish differences between our two numerical models:

- EDGE2 systematically suppresses stellar masses in low-mass systems ( $M_{\star} \leq 10^6 M_{\odot}$ ). This trend is reversed in higher-mass dwarfs ( $M_{\star} \geq 10^6 M_{\odot}$ ), for which  $M_{\star}$  is systematically increased. Sec-

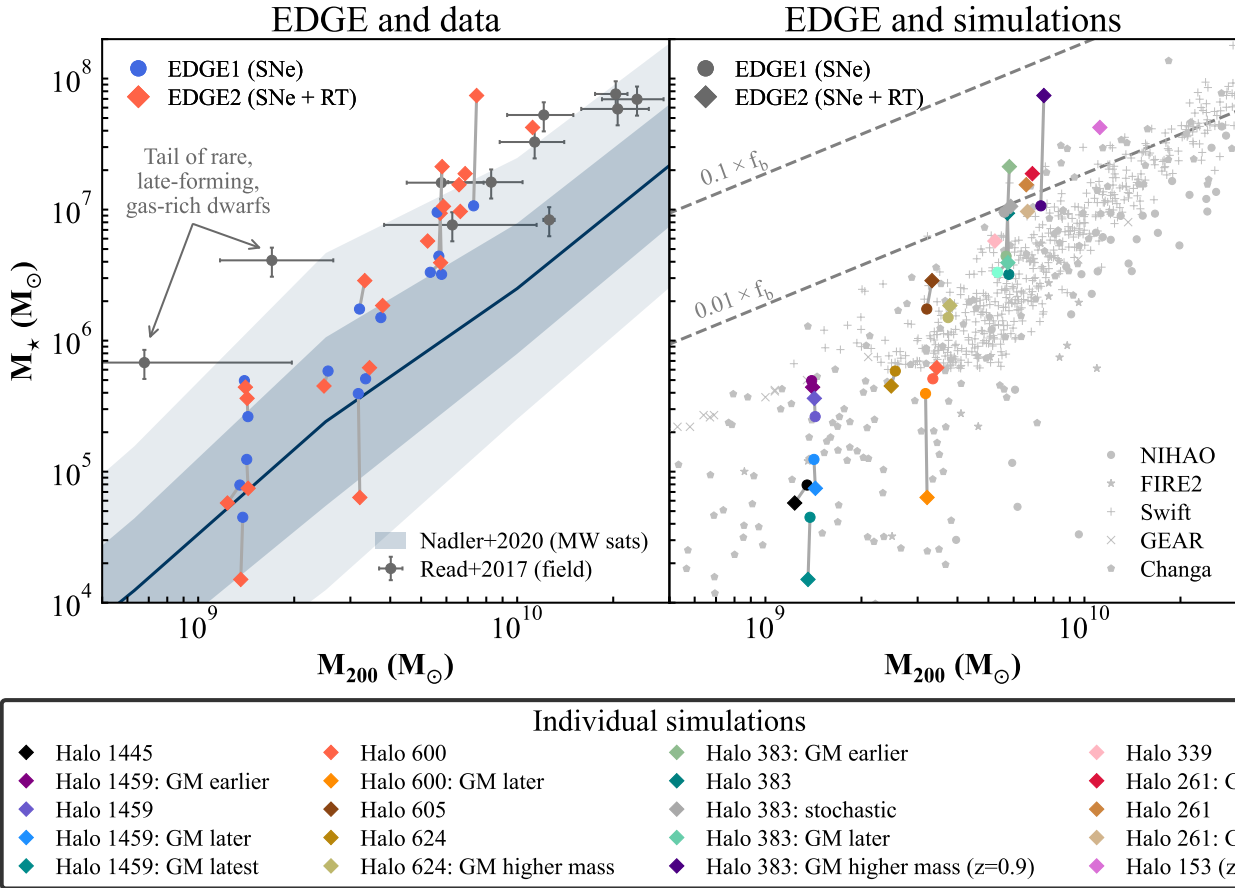


**Figure 2.** Stellar and halo masses of dwarf galaxies simulated with the EDGE1 and EDGE2 models (circles and diamonds, respectively). Both suites are broadly compatible with the stellar-mass-halo-mass relation inferred from Milky Way satellites at the low-mass end (left panel, blue contours; Nadler et al. 2020). Higher-mass objects ( $M_\star \approx 10^7 M_\odot$ ) in EDGE2 (red) closely match the empirical data measured in isolated dwarf irregulars (left panel, grey points; Read et al. 2017). This match to observational data further extends to stellar sizes, gas contents, and stellar and gas-phase metallicities (Figure 6, 7, 8, and 9). The average difference in  $M_\star$  between EDGE1 and EDGE2 is  $\approx 20\%$ , i.e. well converged compared to the scatter in  $M_\star$  at given  $M_{200}$  between different galaxy formation models (right panel, grey points). This is primarily driven by a change in ISM structure (Figure 3) and galactic outflow strength (Figure 4). Section 3.1 discusses the response of individual formation histories (symbols linked with a line and caption).

tion 3.2 and 3.3 show that the inclusion of radiative feedback leads to a fundamentally different structure of the ISM and reduces the efficiency of galactic outflows. This suppression in outflow loading factors is more pronounced at lower masses, driving  $M_\star$  down, and less at higher masses, driving  $M_\star$  up.

- One of our simulated dwarfs (‘Halo 383: GM higher mass’, purple in the right-hand panel) significantly over-shoots the stellar-mass-halo-mass relation, with data for this simulation shown at  $z = 0.9$  when we stopped the simulation due to the numerical cost incurred by the high  $M_\star$ . Little  $M_{200}$  growth is expected after this time. Section 5 shows that, at high  $M_\star$ , the reduced strength of galactic outflows stems from numerical issues leading to increasingly difficult regulation. We stopped ‘Halo 153’ (pink) at  $z = 0.6$  for the same reason.
- Two low-mass galaxies show a large  $M_\star$  suppression with EDGE2 (right panel, ‘Halo 600: GM later’ in orange and ‘Halo 1459: GM latest’ in turquoise). These two objects share the same characteristic of assembling late for their halo masses, from multiple small building blocks during the reionization era each with  $M_{200}(z = 6) \leq 10^8 M_\odot$  that later come together in dry mergers (Rey et al. 2019b, 2020). Each of these small building blocks sees their  $M_\star$  suppressed by radiative feedback, compounding the effect

on the total  $M_\star$  compared to a comparatively massive object at the time of reionization.

### 3.2 The structure of the ISM

Figure 3 shows the difference in ISM structure between models using supernova-only feedback (left) and including radiative feedback (right). For illustrative purposes, we plot the 2D temperature-density distributions averaged over the  $\approx 100$  snapshots along the formation history of ‘Halo 383 (early)’ ( $M_\star \approx 10^7 M_\odot$ ). We pick this galaxy as it has a stable and gas-rich ISM at all times, in both models. But all points highlighted below generalise across the suite.

In both models, we observe similar features in the temperature-density diagram (labelled on plot). Namely, (i) the upper tail of the IGM temperature-density relation (diagonal track at low densities; see McQuinn 2016 for a review); (ii) the distinctive thermal equilibrium curve around  $10^4$  K where radiative cooling balances photo-heating from the external UVB (see e.g. Smith et al. 2017, fig. 8); (iii) the break of this thermal equilibrium when gas starts self-shielding against the UVB; and (iv) high-temperature ( $T \geq 10^5$  K) gas at low densities resulting from SN-driven outflows.

The first notable difference is the warm ( $T \geq 10^4$  K) and dense

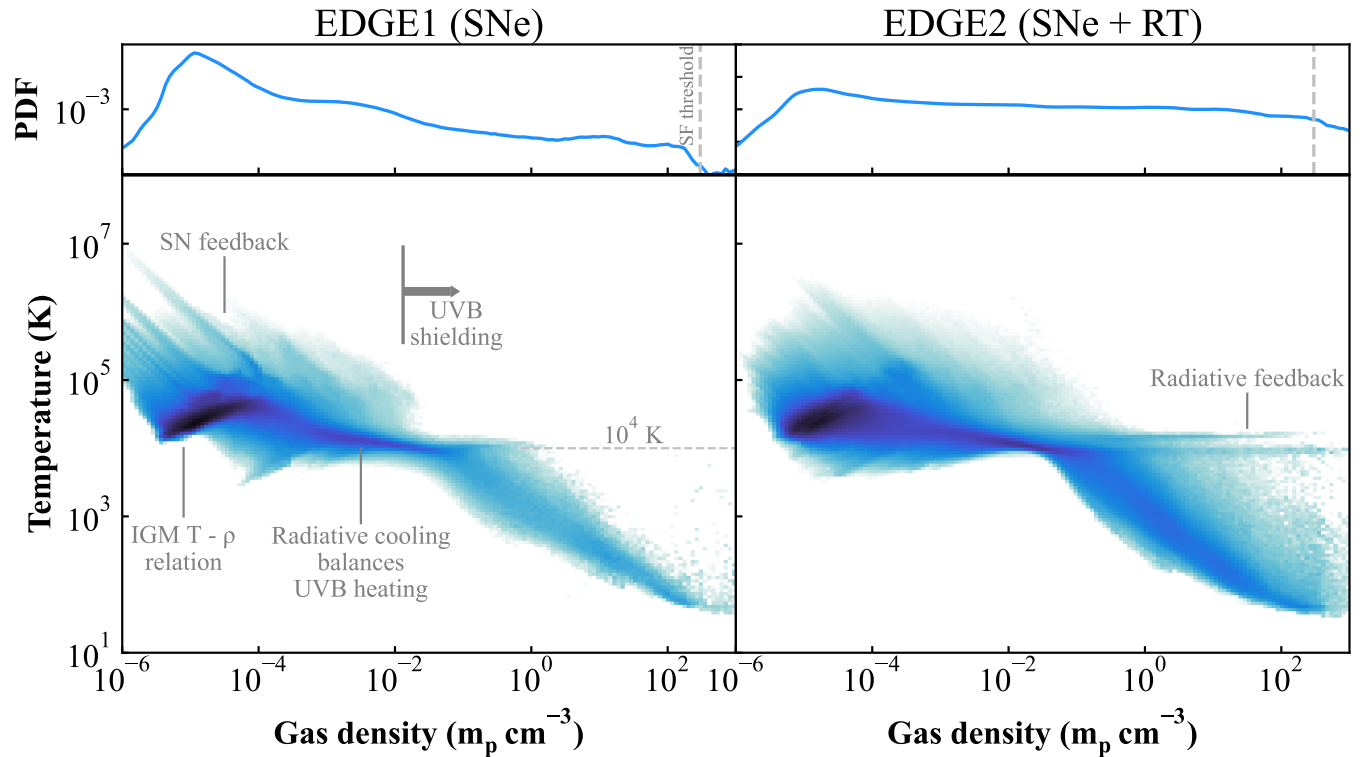


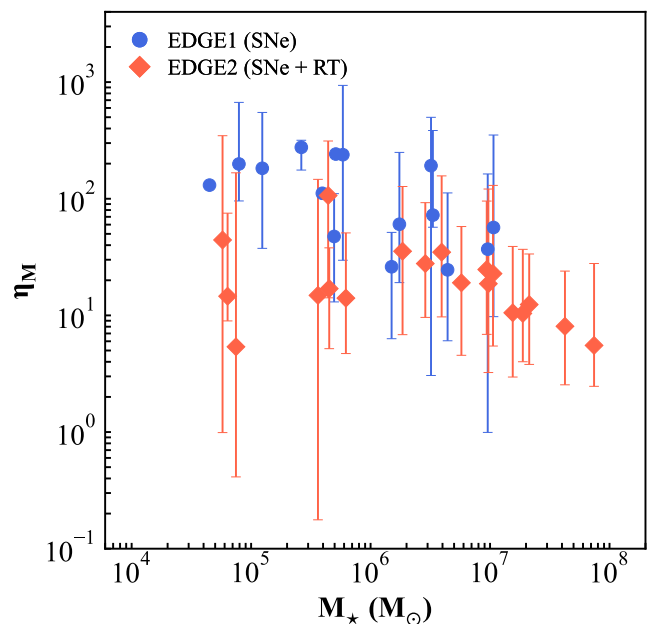
**Figure 3.** Temperature-density diagrams of the ISM of the dwarf galaxy (‘Halo 383 (early)’;  $M_\star \approx 10^7 M_\odot$ ) with the EDGE1 (left) and EDGE2 model (right). The diagrams are 2D mass-weighted PDF averaged over the last 4 billion years of evolution. Many features are shared between models (annotated). The addition of radiative feedback leads to warm ( $T \approx 10^4$  K) and dense ( $n_H \geq 10 \text{ cm}^{-3}$ ) ISM gas. With this change, the ISM is also significantly denser overall (top panels) and the strength of galactic outflows is reduced (Figure 4).

( $\rho \geq 10 m_p \text{ cm}^{-3}$ ) gas present in the EDGE2 model (right panel) and absent in EDGE1 (left panel). This is the direct result of the explicit modelling of radiative feedback in H II regions around stars, ensuring that EDGE2 galaxies now capture a key gas phase for the overall structure of the ISM and its emission lines. The ‘doubled’ horizontal track results from the mixing of photo-ionized gas with the surrounding ISM – the upper track is fully ionized, while the lower track has significant neutral fraction, driving a difference in molecular weight and thus a  $\approx 0.5$  shift in temperature. Part of this mixing is physical, at the edges of H II regions, and part is numerical (Section 5.2).

The second difference is that the ISM is overall denser with non-equilibrium cooling and photo-ionization feedback (top panels show marginalised density PDFs). Surprisingly, this trend extends beyond the density threshold for star formation (dashed lines), with the EDGE2 model maintaining a significant amount of gas at densities above the star-formation threshold ( $\geq 300 m_p \text{ cm}^{-3}$ ; grey dashed) that contrasts with the plummeting PDF in EDGE1. This reflects our numerical choices in the star formation algorithm, which we explore further in Section 5. As we show next, the much denser ISM in EDGE2 correlates with strongly reduced galactic outflows.

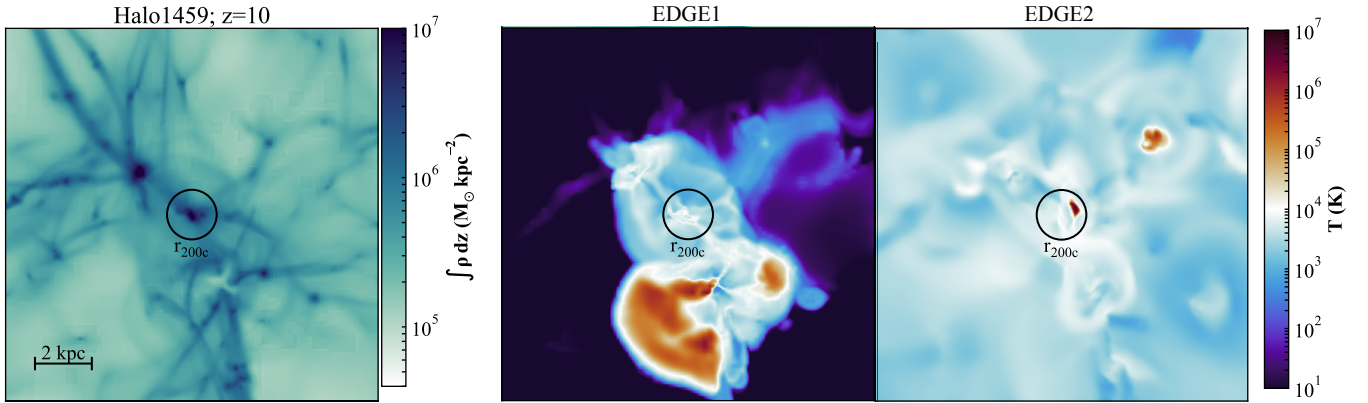
### 3.3 The strength of galactic outflows

Figure 4 shows the gas mass loading factor,  $\eta_M$ , over the cosmological history of each galaxy in the suite as a function of their  $M_\star$ . We define  $\eta_M = \dot{M}_{\text{out}}/\text{SFR}_{10 \text{ Myr}}$ , where the mass outflow rate  $\dot{M}_{\text{out}}$  is measured through a spherical shell centered on the galaxy that spans a radial range between  $0.2 r_{200}$  and  $0.3 r_{200}$  and only includes out-



**Figure 4.** Mass loading factors measured through a spherical shell at  $0.25 r_{200}$  as a function of galaxy stellar mass. Error bars show the 16-84 confidence interval around the median over the cosmological history of each individual dwarf galaxy. Radiative feedback (red) reduces outflow loading factors for every galaxy compared to SN-only feedback (blue). This reduction is up to 1.5 dex for the least massive dwarf galaxies.





**Figure 5.** Gas density integrated along the line of sight (left) and thin slices of the temperature around the same low-mass dwarf galaxy ( $M_\star \approx 10^5 M_\odot$ ) at  $z = 10$ , in EDGE1 (middle) and EDGE2 (right). Accounting for radiative feedback has a dramatic impact beyond  $r_{200}$  (right panel). Radiation efficiently escapes from the dwarf’s small building blocks, heating the volume to  $T \geq 10^3$  K and suppressing inflows and correlated star formation across a large volume. Hot, SN-driven outflows eventually achieve the same effect (middle), but on a timescale longer than radiative feedback.

flowing gas (see also [Rey et al. \(2024a\)](#) for further details).  $\text{SFR}_{10 \text{ Myr}}$  is the star formation rate averaged over 10 Myr. Error-bars show the 16-84 confidence interval of the distribution of  $\eta_M$  values over time, with the median shown as a symbol. Some galaxies for which no saved snapshots have  $\text{SFR}_{10 \text{ Myr}} > 0$  are missing from the plot.

Figure 4 demonstrates that radiative feedback systematically decreases the strength of galactic outflows, reducing their ability to remove mass from the central galaxy. Scatter as a function of time is large, reflecting the stochastic nature of the star formation-feedback cycle, but the suppression is systematic and close to an order of magnitude. Since  $M_\star$  remains close between EDGE1 and EDGE2 (Figure 2), this highlights a fundamental change in the way star formation is regulated. With radiative feedback, gas is prevented from forming stars by gentle heating, rather than being mechanically removed from the centre in blastwaves when considering only SN feedback.

A reduction in the strength of galactic outflows due to radiative feedback is well established in isolated non-cosmological dwarf galaxies (e.g. [Emerick et al. 2018](#); [Smith et al. 2021](#); [Deng et al. 2024b](#); [Andersson et al. 2024](#)) and was previously noted for a single low-mass cosmological dwarf in [Agertz et al. \(2020\)](#). Our simulations extend these findings to a much wider range of masses and highlight trends with host  $M_\star$ .

In particular, the median  $\eta_M$  reduces with increasing  $M_\star$  in the EDGE1 model, as expected from the scaling of SN-driven outflows with  $M_\star$  (e.g. [Muratov et al. 2015](#); [Christensen et al. 2016](#); [Nelson et al. 2019](#); [Mitchell et al. 2020](#); [Pandya et al. 2021](#)). In contrast, EDGE2 sees  $\eta_M$  stay relatively flat over a wide range of  $M_\star$ , even slightly increasing with mass. This is a direct consequence of the different feedback mechanisms at play in the two models.

In EDGE1, there is no rapid feedback mechanism to regulate star formation, the clustering of SNe across all  $M_\star$  is high, and the efficiency of mechanical outflows decreases as the gravitational potential wells get deeper.

In contrast, EDGE2 sees some of the weakest outflows and the strongest outflow suppression compared to EDGE1 in the lowest-mass objects. This reflects the unique regime of very low-mass galaxies that formed all their stars before reionization.

In this case, stellar radiation efficiently escapes the ISM of the small building blocks that will make the  $z = 0$  galaxy but remain spatially distinct at  $z > 10$  (Figure 5, left panel). The radiation propagates outwards much more rapidly than a mechanical outflow, heating up gas to  $T \geq 10^3$  K well beyond the main progenitor’s  $r_{200}$

(right panel)<sup>1</sup>. This in turn suppresses gas inflows and correlated star formation across a much larger volume. This regulation mechanism is fundamentally different to the mechanical outflows driven by SNe in EDGE1 (middle panel). As the galaxies get larger in mass, this effect occurs at ever higher redshift and contributes less to shaping the overall  $M_\star$  of the galaxy.

Lastly, we note that observational values for  $\eta_M$  at  $M_\star \approx 10^7 M_\odot$  have varied from  $\approx 10$  (e.g. [Chisholm et al. 2017](#)), to  $\approx 0.1 - 1$  (e.g. [McQuinn et al. 2019](#); [Xu et al. 2022](#)), to  $10^{-2}$  (e.g. [Marasco et al. 2023](#)), bracketing the values reported here. There are clear limitations in directly comparing the values in Figure 4 to observations. Here,  $\eta_M$  is computed including all gas phases rather than those that are bright in emission lines used to make the measurement. We also use a radius well outside that probed by observations which would likely affect the measured  $\eta_M$  (e.g. [Muratov et al. 2015](#)). Finally, the values in Figure 4 are averaged over the full cosmological history, rather than at a time of star formation when the dwarf galaxy’s gas is observable. A more careful comparison is thus warranted to establish the realism of either EDGE1 and EDGE2 outflows. This will be the focus of a future paper.

## 4 THE EMERGENCE OF DWARF GALAXY SCALING RELATIONS AND THEIR DIFFERENTIATING POWER

### 4.1 The stellar size-luminosity relation

Figure 6 shows the absolute V-band magnitude,  $M_V$ , and projected half-light radius,  $r_{1/2,V}$ , of simulated dwarf galaxies. To obtain these quantities, we compute the luminosity of all star particles within  $r_{200}$  as a function of their mass, age and metallicity according to the single stellar population model of [Bressan et al. \(2012\)](#).  $r_{1/2,V}$  is then obtained along a random line of sight. Simulated properties are compared to observational data from the compilations of [McConnachie \(2012\)](#); [Kirby et al. \(2013, 2014\)](#); [Simon \(2019\)](#) augmented with individual candidates and detections from [Torrealba et al. \(2016, 2018, 2019\)](#); [Homma et al. \(2019, 2024\)](#); [Mau et al. \(2020\)](#); [Bennet et al. \(2022\)](#); [Richstein et al. \(2022\)](#); [Sand et al. \(2022\)](#); [Cerny et al.](#)

<sup>1</sup> Note that the temperatures in Figure 5 are such that most of the hydrogen in the volume remains neutral, thereby not impacting the cosmological timing of hydrogen reionization.

(2023b,c,a); Jones et al. (2023, 2024); McQuinn et al. (2023); Collins et al. (2024); Li et al. (2024); Martinez-Delgado et al. (2024); McNanna et al. (2024); Smith et al. (2023, 2024); Tan et al. (2025). We curate the observational data to use the most recent reference when multiple observations of the same system are available.

Irrespective of the model, nearly all dwarf galaxies are within the observational scatter of  $M_V-r_{1/2,V}$  and there is no clear trend or systematic offset between models. On average, EDGE2 dwarfs are marginally larger than their EDGE1 counterparts, and high-mass EDGE2 dwarfs are systematically brighter in line with their increased  $M_*$  (Figure 2).

Two simulated dwarfs lack direct observed analogues (labelled on plot). In the bottom right, the same dwarf galaxy in both models is an ultra-faint ( $M_V \geq -6$ ) that is also extremely extended ( $r_{1/2,V} \geq 1$  kpc). This large  $r_{1/2,V}$  is driven by the specific assembly history of this galaxy that sees its stellar component built from the mergers of small building blocks that deposit stars on wide orbits (see Rey et al. 2019b for details). As discussed in Section 3.1, photo-ionization feedback is particularly efficient in these small building blocks, and this object becomes even more diffuse in the EDGE2 model. In both cases, the lack of observational counterpart can be explained by their central surface brightnesses being beyond currently-observable capabilities ( $\mu_{0,V} > 31$  mag arcsec $^{-2}$ ). Such dwarfs should be revealed by forthcoming surveys such as on the Vera Rubin C. Observatory.

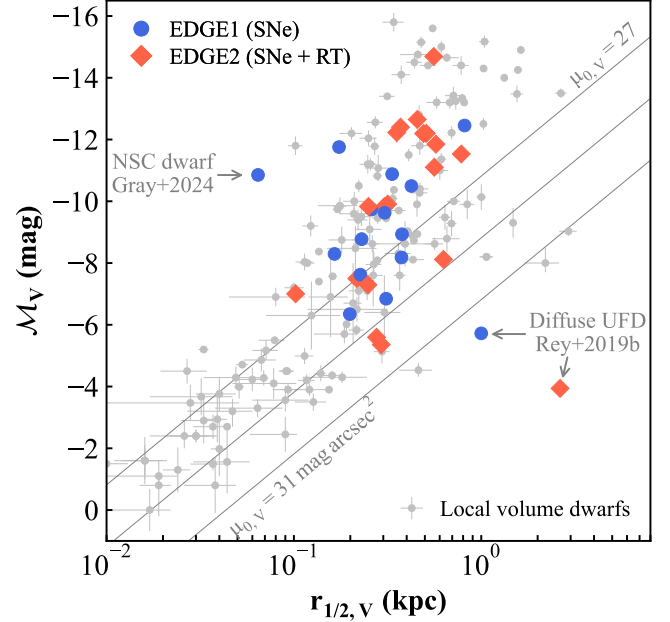
In the left-hand corner, one EDGE1 dwarf (blue point) has a particular formation history that leads to a compact nuclear star cluster that dominates the light of the galaxy. This galaxy shares observational characteristics with ultra-compact dwarfs and nuclear star clusters not included in Figure 6 (see Gray et al. 2024 for a discussion). Due to the reduced outflow strength and less clustered star formation, this galaxy does not qualify as a nuclear star cluster in EDGE2.

Our results highlight the natural emergence of the  $M_V-r_{1/2,V}$  scaling relation, in both median and scatter, from our cosmological modelling. This emergence is robust to a large change in galaxy formation modelling from EDGE1 to EDGE2. Such convergence hints that, if stellar masses are reasonably predicted at a given  $M_{200}$ , the  $M_V-r_{1/2,V}$  relation and its scatter follow from the diversity of cosmological assemblies. This in turn brings confidence that this relation can be well predicted with physics-informed semi-analytical arguments applied to dark-matter-only simulations (S. Nigudkar et al. in prep.).

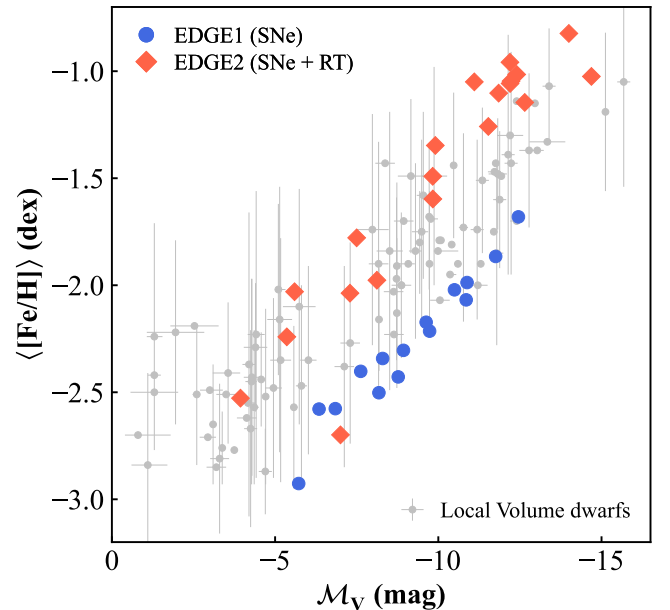
## 4.2 The stellar mass-metallicity relation

Figure 7 shows the  $M_V-\langle[\text{Fe}/\text{H}]\rangle$  relation where  $\langle[\text{Fe}/\text{H}]\rangle$  is the average stellar iron abundance. We derive  $[\text{Fe}/\text{H}]$  for each stellar particle within  $r_{200}$  from their iron mass fractions and compute  $\langle[\text{Fe}/\text{H}]\rangle$  as the mass-weighted average (see Escala et al. 2018, eq. 3 and 4). Observed data is compiled from Kirby et al. (2013, 2014); Simon (2019) augmented and updated with data from Kirby et al. (2017, 2020); Li et al. (2017, 2018); Longeard et al. (2018); Fritz et al. (2019); Ji et al. (2019, 2021); Collins et al. (2020, 2021); Pace et al. (2020); Taibi et al. (2020); Wojno et al. (2020); Jenkins et al. (2021); Chiti et al. (2021, 2022); Bruce et al. (2023); Charles et al. (2023); Cerny et al. (2023a); Smith et al. (2023); Hansen et al. (2024); Heiger et al. (2024); Kvasova et al. (2024); Tan et al. (2025). Data error-bars show the dispersion around  $\langle[\text{Fe}/\text{H}]\rangle$  (when available) rather than measurement errors on the mean.

Both EDGE1 and EDGE2 models accurately track the slope of the  $M_V-\langle[\text{Fe}/\text{H}]\rangle$  relation and are within the observational scatter. However, EDGE1 dwarfs populate the lower end of observed points over



**Figure 6.** Absolute V-band total magnitude of simulated dwarf galaxies against their V-band half-light radius. With both models (red and blue), simulated dwarf galaxies populate the observational scatter observed around the Local Volume (grey points; error-bars showing the dispersion around the median) showcasing the limited power of stellar sizes in discriminating between galaxy formation models. Three exceptions lack an observational counterpart (labelled) but do not pose significant challenges to either model (see text discussion).



**Figure 7.** Absolute total V-band magnitude of our simulated galaxies against the average iron content of their stars. Both models track the slope of the mass-metallicity relation, but are offset with one another due to the changes in metal production tables and feedback physics.

the range of  $M_V$ , while EDGE2 dwarfs populate the upper end. The origin of the  $\approx 0.5$  dex offset between models is two-fold. First, the EDGE2 model produces  $\approx 2.5$  more iron per stellar mass formed than EDGE1 (Figure 1). And second, the inclusion of radiative feedback leads to a more gentle regulation of star formation with weaker galactic outflows (Section 3), and thus metal retention in the ISM. These two effects compound one another, with both iron production and retention increased in the EDGE2 ISM, in turn leading to higher  $\langle[\text{Fe}/\text{H}]\rangle$ .

These results cement the  $M_V$ - $\langle[\text{Fe}/\text{H}]\rangle$  relation as a sensitive probe of star formation and stellar evolution physics at low metallicities (see also Agertz et al. 2020; Prgomet et al. 2022; Sanati et al. 2023). The normalization at a given  $M_V$  is in particular directly related to the strength of galactic outflows in dwarf galaxies, while the slope emerges from the cosmological relation between stellar mass and halo mass. A way to more strongly discriminate between feedback models is thus to increase the precision of  $\langle[\text{Fe}/\text{H}]\rangle$  measurements in dwarf galaxies. This will occur in the forthcoming years as more stellar abundances per dwarf galaxy become available (e.g. Skúladóttir et al. 2023).

Another promising route is to combine  $M_V$ - $\langle[\text{Fe}/\text{H}]\rangle$  with more observables of the star formation and feedback cycle. Given the sensitivity of iron abundances, further ratios beyond chemical elements are likely to provide complementary constraints on metal production and retention. We will use the extended number of chemical elements tracked in EDGE2 to explore this in future work. Next, we focus on the gas contents and gas-phase metallicity of our simulated dwarf galaxies.

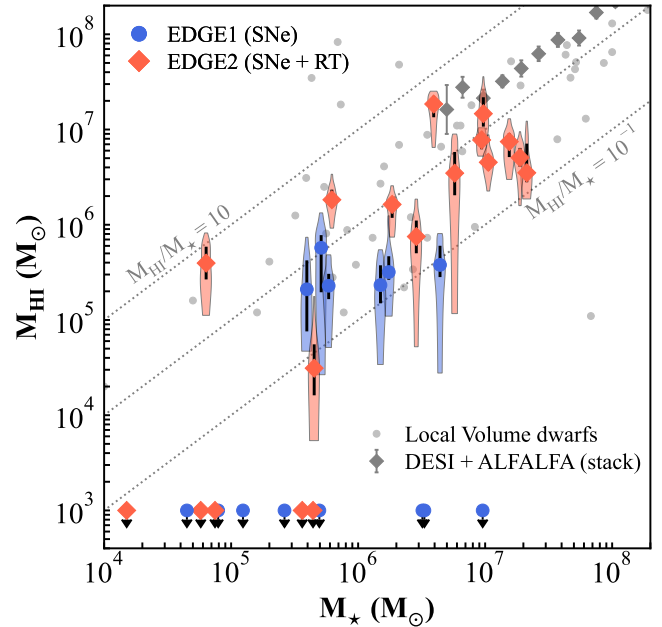
### 4.3 The gas content of dwarf galaxies

Figure 8 shows the  $M_\star - M_{\text{H I}}$  relation for our simulated dwarf galaxies, where  $M_{\text{H I}}$  is the total H I mass within  $r_{200}$  (see Rey et al. 2022 for how we derive  $M_{\text{H I}}$  in EDGE1, while natively tracks out-of-equilibrium H I fractions). Violins in Figure 8 show the distribution of  $M_{\text{H I}}$  over the last 4 billion years (symbols and lines showing the medians and 16-84 confidence intervals, respectively). This is long enough to average over the time variability due to stellar feedback, but short enough that  $M_\star$  does not vary significantly (e.g. Rey et al. 2022).

Both models predict a similar structure for the  $M_\star - M_{\text{H I}}$  relation, with the most distinct feature being a bimodality between gas-deficient dwarfs with vanishing H I contents (upper limits at the bottom) overlapping in  $M_\star$  with gas-rich systems. This bimodality arises from the interplay between the UVB and stellar feedback which regulate the gas and H I contents, and the diversity of possible mass-growth histories in a  $\Lambda$ CDM universe (Rey et al. 2022; see also e.g. Benitez-Llambay & Frenk 2020; Benitez-Llambay & Fumagalli 2021; Kim et al. 2024).

For dwarf galaxies with measurable H I contents, both models produce dwarf galaxies within the observational scatter from a compilation of individual gas-rich field dwarfs (McConnachie 2012; Cole et al. 2014; McQuinn et al. 2015, 2020, 2021; Sand et al. 2015; Adams & Oosterloo 2018; Brunner et al. 2019; Janesh et al. 2019; Hargis et al. 2020; Bennet et al. 2022; Xu et al. 2023; grey circles). In the case of the EDGE2 model, this agreement is striking for  $M_\star \approx 10^7 M_\odot$  where simulated dwarfs cluster around the  $M_\star - M_{\text{H I}}$  relation from Scholte et al. (2025) that combines DESI and ALFALFA (grey diamonds) to stack a mass-complete sample. Note that the error-bars on the stack show the error on the median, not the expected population scatter which can be read from individual measurements.

Across the suites, EDGE2 galaxies are on average more H I-rich than



**Figure 8.** H I and stellar masses of our simulated dwarf galaxies in each model. The structure of the  $M_\star - M_{\text{H I}}$  is robust to our change of model, with a bimodal structure at the low-mass end and significant time variability in H I content due to stellar feedback (violins show the distribution over the last 4 Gyrs). Both models are within the observed scatter at low masses (grey circles; see text for the compilation of individual detections), with EDGE2 approaching the  $M_\star - M_{\text{H I}}$  relation of a stacked mass-complete sample at higher masses (grey diamonds; Scholte et al. 2025).

EDGE1 galaxies at similar  $M_\star$ , as expected since radiative feedback dampens galactic outflows (Figure 4). Similarly, both models predict substantial variability (violins), but  $M_{\text{H I}}$  is more stable over time in the EDGE2 model (the extent of the 16-84 confidence interval is 53% smaller on average). And an even more notable difference is the lack of H I-deficient, higher-mass dwarf galaxies ( $M_\star \geq 10^6 M_\odot$ ) in EDGE2. Runaway star formation and highly clustered SN feedback during mergers can vacate the whole H I reservoir and self-querch a dwarf galaxy, while a more gentle, radiative regulation of star formation allows them to retain more gas.

We conclude that the exact shape of the bimodality at low  $M_\star$ , the median  $M_{\text{H I}}$  at a given  $M_\star$  and the scatter around this median due to time variability are all sensitive to the efficiency with which dwarf galaxies drive galactic outflows. This is promising for future comparisons with forthcoming radio surveys (e.g. Wallaby, Koribalski et al. 2020; Apertif-Medium deep, van Cappellen et al. 2022). But the fact that the structure and the key features of the  $M_\star - M_{\text{H I}}$  relation robustly emerge from our modelling, despite large changes in the cooling and heating physics of the EDGE model, highlight that constraining power will only be unlocked by leveraging large populations of dwarf galaxies. This requires developing a new generation of semi-analytical models building on the insights presented here to generate large statistical samples of H I dwarfs, which we will present in future work (S. Hutton et al. in prep.).

### 4.4 The gas-phase mass-metallicity relation

Figure 9 shows the  $M_\star$ - $\langle 12 + \log(\text{O}/\text{H}) \rangle$  relation at  $z = 0$ , where  $\langle 12 + \log(\text{O}/\text{H}) \rangle$  is the mass-weighted average oxygen metallicity in the gas phase. To compute  $\langle 12 + \log(\text{O}/\text{H}) \rangle$ , we select gas within  $2r_{1/2,V}$

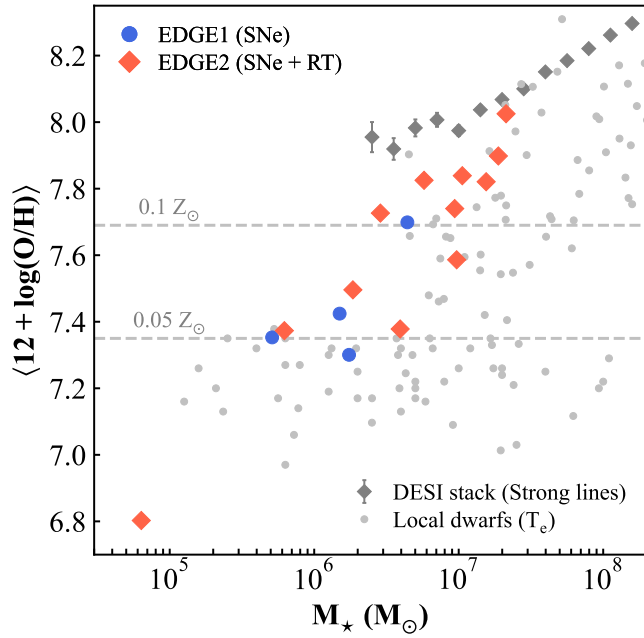


**Figure 9.** Stellar mass versus gas-phase oxygen metallicity for simulated dwarf galaxies that have formed new stars within the last 4 million years. Both models track the slope of the mass-metallicity relation and are broadly compatible with individual measurements of metal-poor, low-mass dwarfs (grey). EDGE2 dwarfs (red) are slightly more metal-rich at a given stellar mass and populate the upper end of the observational scatter. But these effects are smaller than uncertainties arising from measuring gas-phase metallicities with different calibration methods (strong-line calibration as diamonds, direct-method as circles).

of dwarf galaxies that have formed new stars in the last 4 billion years, as measured data of oxygen metallicity almost invariably rely on ionized emission lines in H II regions. We do not account for dust depletion which should be small at our low metallicities.

Observed data (grey circles) shows measurements of individual  $z = 0$  dwarf galaxies compiled by Yates et al. 2020 and J. Breneman et al. in prep. All these points measure the electron temperature  $T_e$  from auroral lines to derive  $\langle 12 + \log(\text{O}/\text{H}) \rangle$ . We omit their error-bars for visual clarity. We also show the stack of emission-line-selected dwarf galaxies from DESI (Scholte et al. 2025; pentagons) with metallicities derived from strong-line calibration (Nakajima et al. 2022).

Both EDGE1 and EDGE2 are broadly within the scatter of individual measurements of gas-phase metallicities and track the slope of the relation. On average, EDGE2 dwarfs are slightly more oxygen rich ( $\approx 0.1$  dex) at similar stellar masses than EDGE1 dwarfs. This much smaller upshift than for stellar  $\langle [\text{Fe}/\text{H}] \rangle$  ( $\approx 0.5$  dex) is readily explained by the difference in chemical elements used for the observable. While the weaker galactic outflows in EDGE2 increase oxygen retention in the ISM (driving  $\langle 12 + \log(\text{O}/\text{H}) \rangle$  higher), oxygen production per stellar mass formed is more than halved with our updated CCSNe yields (Figure 1), driving  $\langle 12 + \log(\text{O}/\text{H}) \rangle$  lower. When combined, this leads to a small change in the overall  $\langle 12 + \log(\text{O}/\text{H}) \rangle$  of our galaxies.

The EDGE2 model predicts one example of a very low-mass  $M_\star \leq 10^5 M_\odot$ , very metal-poor, star-forming dwarf galaxy (bottom left corner). This object (‘Halo 600: GM Later’) is quenched by cosmic reionization early on, and achieves a high-enough dynamical mass to re-ignite star formation particularly late ( $z = 0.2$ , Rey et al.

2020). The delayed growth drives down  $M_\star$  and  $\langle 12 + \log(\text{O}/\text{H}) \rangle$  along the slope of the mass-metallicity relation. This highlights the possibility for low-mass dwarf galaxies even more oxygen-deficient than currently known forming through such rare assembly histories.

We conclude that, like for the stellar-phase mass metallicity relation (Figure 7), the normalization of the gas-phase mass metallicity is sensitive to the galaxy formation assumptions made. However, given the implementation choices between EDGE1 and EDGE2, the shifts observed ( $\approx 0.1$  dex) are smaller than systematic uncertainties in metallicity measurements. This is illustrated by the  $\approx 0.3$  dex offset between individual and stacked measurements (grey circles and diamonds). Such offset is of the magnitude expected given their distinct metallicity calibration (strong line method validated with ‘semi-direct’ observations, versus ‘semi-direct’ and ‘direct’ auroral measurements; see e.g. Kewley & Ellison 2008; Yates et al. 2020 for a discussion). And shifts in  $\langle 12 + \log(\text{O}/\text{H}) \rangle$  of  $\approx 0.1$  dex are also well within the uncertainties of comparing direct-method measurements to simulation values (e.g. Cameron et al. 2023). A more detailed exploration is thus warranted to establish the precise constraining power of the gas-phase mass-metallicity relation on feedback models in the dwarf galaxy regime.

## 5 NUMERICAL LIMITATIONS AND REMAINING UNCERTAINTIES IN THE EDGE2 MODEL

The comparison between new and previous generation of EDGE simulations has revealed impressive convergence in observables (Section 4) but fundamentally different ISM and outflow structures (Section 3). In this section, we discuss the sensitivity of these comparisons to key uncertainties, discuss numerical limitations of our radiative simulations, and highlight key systematics yet to be quantified when modelling small dwarf galaxies.

### 5.1 Direct numerical tests

To explore uncertainties in our modelling, we re-simulate multiple times a dwarf galaxy midway through the mass-range of our sample (‘Halo 605’;  $M_\star \approx 10^6 M_\odot$ ). This dwarf survives reionization and maintains star formation for a Hubble time, providing a long baseline to compare between model inputs. Figure 10 shows how  $M_\star$  and  $\langle [\text{Fe}/\text{H}] \rangle$  respond to variations in key numerical and physical parameters that we detail next.

#### 5.1.1 Chaotic noise and stochasticity

We start by quantifying the intrinsic noise level and stochasticity in our model. The chaotic nature of galaxy formation combined with finite numerical precision can lead to divergent evolution from the same initial conditions (see e.g. discussion in Keller et al. 2019; Genel et al. 2019).

To quantify the magnitude of this noise term, we re-simulate our test galaxy twice, each time seeding a different truncation error. We achieve this by re-simulating the same initial condition on a different number of cores, which changes the order of arithmetic operations and their truncation errors when communicating across a supercomputer’s network. The simulations were stopped at  $z = 0.5$  to limit the computational cost.

The envelopes (left panels) around the fiducial EDGE2 run (red) in Figure 10 show the extent of the differences in  $M_\star$  and  $\langle [\text{Fe}/\text{H}] \rangle$  spanned by these 2 additional stochastic re-simulations. At early times, when few stellar particles are present, stochasticity effects can



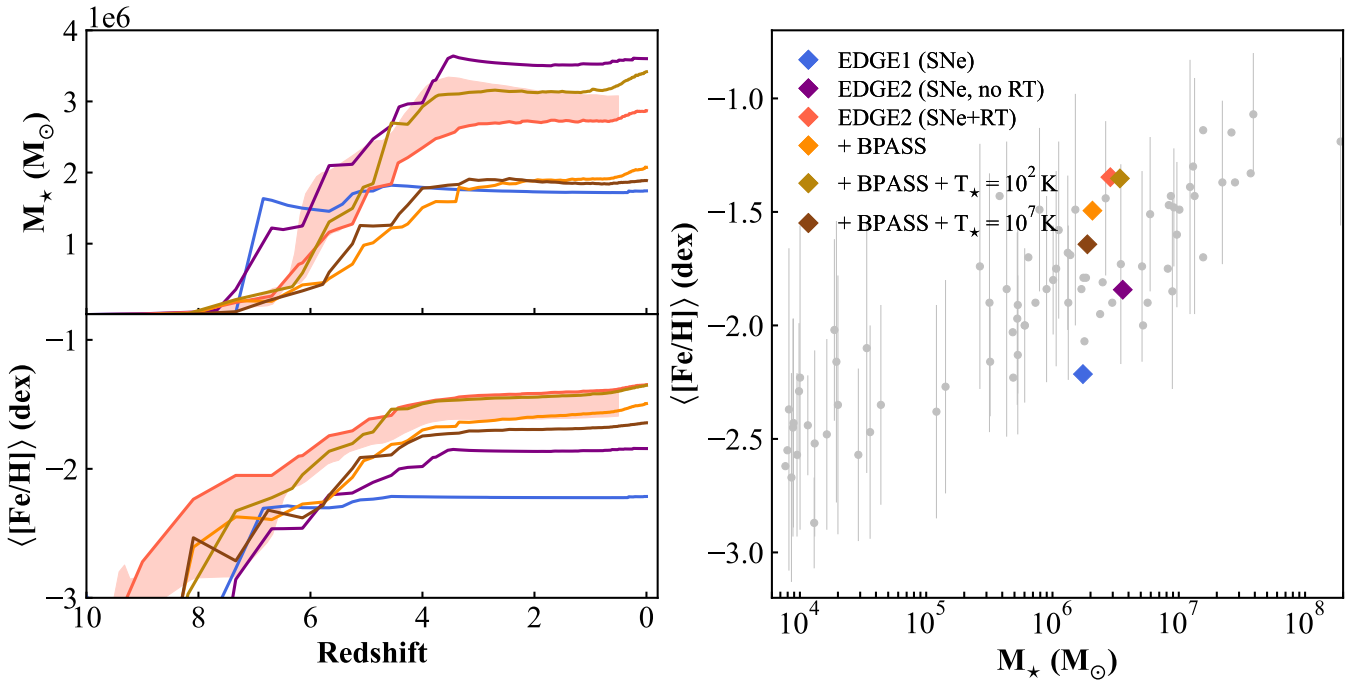


**Figure 10.** Stellar mass and metallicity growth over cosmic time (left) and at  $z = 0$  for multiple versions of the same dwarf galaxy (‘Halo 605’) varying input parameters. The increased iron production between EDGE1 and EDGE2 (see Figure 1) drives a  $\approx 0.4$  dex increase in  $\langle [\text{Fe}/\text{H}] \rangle$  at  $z = 0$  (blue vs purple). Further adding radiative feedback (purple vs red) increases  $\langle [\text{Fe}/\text{H}] \rangle$  by another  $\approx 0.5$  dex by enhancing iron retention in the ISM. Varying the SED (orange versus red) and parameters of the star formation algorithm (gold and brown versus orange) has a smaller overall effect, but modulates the clustering of star formation and the ability to drive more or less powerful outflows. Intrinsic stochasticity due to chaotic noise in the simulations is small compared to these shifts (red envelopes).

be substantial, but the different simulations have converged with one another by  $z \approx 6$ .

Averaging over the three simulations, we find  $M_\star(z = 0.5) = 2.85^{+0.06}_{-0.15} \times 10^6 M_\odot$  and  $\langle [\text{Fe}/\text{H}] \rangle(z = 0.5) = -1.45^{+0.04}_{-0.10}$ . Such differences are small compared to the factor-of-a-few changes going from the EDGE1 to the EDGE2 model. They also remain small compared to other input variations that we explore next.

Admittedly, 3 simulations is a limited sample size to make statistical statements. The numerical costs of these simulations make a wider exploration impractical, but we note that the magnitude of the scatter in  $M_\star$  is comparable to previous findings in the EDGE1 context (Pontzen et al. 2021). We conclude that chaotic stochasticity, while present, plays a small role in the trends and shifts in observables discussed in this paper.

### 5.1.2 Radiative feedback versus other inputs

In addition to radiative feedback, the EDGE2 model makes significant updates to the chemical enrichment modelling and SN feedback budget (Figure 1). To isolate the effect of these changes on  $\langle [\text{Fe}/\text{H}] \rangle$ , we re-simulate our test dwarf galaxy in the EDGE2 model turning off non-equilibrium cooling and radiative feedback.

Comparing this new run to the original EDGE1 version in Figure 10 (blue against purple, respectively), we find a  $\approx 2\times$  increase in  $M_\star$  and  $\approx 0.4$  dex increase in  $\langle [\text{Fe}/\text{H}] \rangle$ . Conversely, contrasting runs with and without radiative feedback (purple versus red, respectively),  $M_\star$  is decreased by  $\approx 20\%$  while  $\langle [\text{Fe}/\text{H}] \rangle$  further increases by another  $\approx 0.5$  dex. All of these shifts are large compared to chaotic stochasticity (Section 5.1.1).

To summarize, our updates to the IMF and to the chemical enrichment modelling between EDGE1 and EDGE2 drives roughly half

of the total increase in  $\langle [\text{Fe}/\text{H}] \rangle$  at  $z = 0$ . The other half is due to radiative feedback promoting metal retention through weaker outflows. It is thus clear that both of these inputs play an important role in setting the normalization of the stellar mass–metallicity relation. In the future, we will provide a much more detailed exploration of CCSNe yield models and further variations of the SNeIa inputs (E. Andersson et al. in prep.)

### 5.1.3 The spectral energy distribution

Another key input to radiative feedback is the choice of the SED for stellar populations. Figure 10 shows the response of our test dwarf galaxy when swapping from our fiducial SED (Bruzual & Charlot 2003, red) to a harder and more ionizing BPASS2.2 SED (Stanway et al. 2016; orange) that takes into account binary populations of massive stars.

As expected with increasing the hardness and number of ionizing photons per stellar population, the dwarf galaxy is  $\approx 30\%$  fainter overall and  $\approx 0.25$  dex more metal poor. These shifts are more modest than the other numerical choices we have explored, but remain larger than the intrinsic stochasticity. We conclude that the choice of SED is a subdominant parameter in setting the stellar masses and metallicities. At present, we therefore settle on the fiducial SED for the EDGE2 suite as a whole.

### 5.1.4 The coupling between photo-ionization feedback and the star formation algorithm

Figure 3 shows that the EDGE2 ISM has a longer high-density tail, with significant gas staying above our density threshold for star formation. This stems from the combined conditions that star-forming gas has

to be dense and cold, with our fiducial setup restricting star-forming gas to have  $T < T_\star = 1000$  K (Section 2.4).

Figure 10 shows two more re-simulations of our test dwarf galaxy lowering and raising this temperature threshold, while keeping the density threshold the same at  $300 m_p \text{ cm}^{-3}$ . The input SED in all cases is taken to be `BPASS2.2` (Section 5.1.3).

Lowering  $T_\star$  to 100 K (gold) increases the stellar mass by  $\approx 60\%$  compared to the fiducial value with the same SED (orange), despite having made the conditions to form stars more restrictive. This is combined with an increase in  $\langle [\text{Fe}/\text{H}] \rangle$  by  $\approx 0.2$  dex, indicating increased metal retention and weaker outflows. Effectively removing  $T_\star$  by increasing it to  $10^7$  K (brown) lowers  $M_\star$  and  $\langle [\text{Fe}/\text{H}] \rangle$ .

We show in Appendix C that  $T_\star$  in fact controls the clustering of star-formation and SNe events. Following a star formation event, the dense gas surrounding the newborn stellar particle is immediately heated to  $T \geq T_\star = 10^3$  K by radiative feedback. Any gas in the immediate vicinity of a star-forming event is thus prevented from forming new stars, introducing an effective limit on the clustering of star formation. Figure C2 shows how lowering  $T_\star$  compounds this effect, leading to star formation and supernova events forming at ever-increasing densities and in turn reducing the efficiency of galactic outflows at clearing this high-density gas.

This behaviour reflects the difficulties of modelling stellar photo-heating, even at the high resolution of these simulations. If all processes around H II regions are captured, a star formation site would remain a mixture of cold gas below  $T_\star$  allowed to form stars, and of warm photo-heated gas above  $T_\star$  prevented from star formation. If, however, resolution is limited, this multiphase star formation site is numerically mixed into a partially-neutral, lukewarm phase. Restricting star formation to cold gas then unphysically shuts down correlated star formation. As shown in Appendix B, our simulations are in this regime of partially-resolved radiative feedback, for which removing  $T_\star$  provides a way to rebuild correlation between SF events that have been spuriously erased.

### 5.1.5 Convergence with dark matter resolution

Using a similar `EDGE` setup with non-equilibrium cooling and radiative transfer, Agertz et al. (2020) demonstrated that our fiducial dark matter resolution ( $m_{\text{DM}} \approx 950 M_\odot$ ) resolves well the cooling and ISM of small dark matter haloes. Re-simulating a low-mass object with 8 times more dark matter particles while keeping the spatial resolution fixed, they found well converged stellar masses, sizes and iron metallicities (compare ‘Fiducial+RT’ to ‘Hires + RT’ in their Table 2).

We repeat this experiment with the updated `EDGE2` model, re-simulating one of our low-mass object, ‘Halo 1459 (earlier)’, improving  $m_{\text{DM}}$  from  $940 M_\odot$  to  $118 M_\odot$  and keeping  $\Delta x = 3$  pc. At  $z = 0$ ,  $M_\star$  changes from  $7.4 \times 10^4 M_\odot$  to  $7.9 \times 10^4 M_\odot$ ,  $r_{1/2, \text{V}}$  from 230 to 190 pc, and  $\langle [\text{Fe}/\text{H}] \rangle$  from -2.03 to -2.11. These shifts are comparable in magnitude to those induced by chaotic stochasticity (Section 5.1.1) and we conclude that the observables presented in this work are robust to the choice of dark matter resolution.

## 5.2 The impact of partially-resolved Strömgren spheres

In Appendix B, we show that at our resolution ( $\Delta x = 3$  pc) the Strömgren radii,  $R_S$ , of photo-ionized H II regions from radiative feedback events are only partially resolved. This is a key numerical limitation of our simulations, which has a number of consequences we discuss here.

First, an unresolved Strömgren radius around a stellar cluster will mix two gas regions, one warm and ionized, one cold and neutral, into a single element that is lukewarm and partially ionized. Such out-of-equilibrium dense, warm and mostly-neutral gas cools very efficiently through collisional excitation, generating a source of numerically-induced cooling that is yet to be fully understood (e.g. Deng et al. 2024a).

Furthermore, this numerically-mixed gas from unresolved Strömgren radii interacts with the temperature threshold for star formation (Section 5.1.4), preventing star formation in larger regions of space than should physically be allowed. This then suppresses the clustering of star formation and subsequent CCSNe feedback. In turn, this may mean that `EDGE2` outflows are somewhat too weak, but we stress that the impressive agreement with observed scaling relations (Section 4) makes it unclear whether this is a significant issue. In future work, we will quantitatively compare the characteristics of our outflows to observations to obtain an orthogonal constraint (e.g. McQuinn et al. 2019; Xu et al. 2022; Marasco et al. 2023).

How to best address the numerical losses from under-resolved Strömgren spheres is a key open question for the next-generation of radiation-hydrodynamics dwarf galaxy simulations.

An obvious solution is to simply increase numerical resolution until  $R_S$  is resolved, providing a robust test of the physical-vs-numerical reduction in the strength of galactic outflows. Such an endeavour will be computationally demanding, but could already be achieved using super-Lagrangian strategies around star formation events similar to those implemented for black hole accretion (e.g. Curtis & Sijacki 2015; Beckmann et al. 2018; Anglés-Alcázar et al. 2021). However, given that numerical resolution is already at  $\approx 3$  pc across the ISM, going further will likely require algorithmic improvements to, for example explicitly sample the IMF in star formation events and inject radiative feedback star by star rather than as a population average as is done here.

An alternative approach could be to keep the resolution unchanged, but revise subgrid algorithms. For example, one can probabilistically draw the ionization fraction of H II regions when they are under-resolved (Hopkins et al. 2022), or allow stars to form at either lower densities or in more massive particles to boost their ionizing power and thus  $R_S$  (e.g. Katz et al. 2024). Future studies quantifying the effects of these assumptions on dwarf galaxy properties will be crucial.

Lastly, under-resolved Strömgren spheres also have an important impact when comparing simulated and observed dwarf galaxies. Since cooling is efficient in the spurious warm-dense, partially-neutral ISM phase, it leads to much brighter emission lines luminosities compared to what should be the true luminosity of the dwarf galaxy. This requires corrections to obtain accurate estimates (e.g. Katz et al. 2023; Ejdetjärn et al. 2024) and will be a key problem to solve when comparing `EDGE2` data with observed emission lines.

## 5.3 Untested theoretical uncertainties

Beyond the numerical limitations and parameter exploration discussed above, there remain several astrophysical inputs needed for cosmological zoom simulations whose impact we are yet to explore.

For example, the choice of the IMF, of the UVB, and of the chemical yields all have consequences for the cooling, heating and metallicity balance of the ISM. We have not yet been able to test all of these independently within the new `EDGE2` model, but many of these uncertainties have been explored in previous iterations of the `EDGE` model. In particular, Rey et al. (2020) discusses the consequences of varying the redshift at which cosmic reionization happens (see

also Benitez-Llambay & Frenk 2020; Katz et al. 2020), Prgomet et al. (2022) investigates the impact of a metallicity-dependent IMF, while Andersson et al. (2025) shows convergence tests against a new feedback budget sourced by individual stars. Future work will also present a thorough exploration of the impact of yield inputs on EDGE galaxy chemistry (E. Andersson et al. in prep.)

And despite the milestone advance of including non-local stellar radiative input, other galaxy formation processes remain missing from this breed of EDGE dwarf galaxies. Exotic stellar evolution tracks (e.g. hypernovae, pair-instability supernovae, variable-energy supernovae, metal-free primordial stars) can have dramatic effects on such small dwarf galaxies (e.g. Jeon et al. 2017, 2021; Gutcke et al. 2022; Sanati et al. 2023) and leave distinct traces in their chemistry. The growing abundance of evidence of active galactic nuclei in dwarf galaxies (see e.g. Reines et al. 2013, 2020; Burke et al. 2022; Davis et al. 2022; Mezcua & Sánchez 2024 and summary in Wasleske & Baldassare 2024) and their associated outflows (e.g. Liu et al. 2020, 2024) calls for the inclusion of black hole processes at this mass scale, although different implementations do not converge on their importance over a Hubble time (e.g. Koudmani et al. 2021, 2022; Sharma et al. 2023; Arjona-Galvez et al. 2024). Similarly, cosmic ray feedback provides a different avenue to regulate star formation, with its efficiency in faint dwarf galaxies now starting to be quantified (e.g. Martin-Alvarez et al. 2023). Future extensions of the EDGE project will explore these avenues.

## 6 SUMMARY AND CONCLUSION

We present new EDGE radiation-hydrodynamics cosmological zoomed simulations covering dwarf galaxy formation from the ultra-faint to the dwarf irregular regime ( $10^9 \leq M_{200} \leq 10^{10} M_{\odot}$ ;  $10^4 \leq M_{\star} \leq 10^8 M_{\odot}$  at  $z = 0$ ). Our combination of a uniformly high resolution ( $\approx 3$  pc,  $m_{\text{DM}} \approx 950 M_{\odot}$ ), a large sample size (15 galaxies) and a detailed stellar feedback modelling (resolved SN feedback and explicit radiative feedback) is unprecedented. Leveraging previous-generation EDGE simulations with similar resolution but without radiative feedback, we systematically compare the response of dwarf galaxy observables to this change in physical modelling.

The addition of radiative feedback leads to a fundamentally different ISM structure (Figure 3) in which star formation and gas accretion are increasingly regulated by radiative heating from massive stars, rather than mechanical removal from the halo centre. This change in regulation mode leads to a strong suppression of the mass outflow rates in dwarf galaxies over their cosmological history (Figure 4). These findings reaffirm that radiative feedback reduces galactic outflows in dwarf galaxies, extending previous results (Agertz et al. 2020 for a single cosmological dwarf and e.g. Emerick et al. 2018; Smith et al. 2021; Deng et al. 2024b; Andersson et al. 2024 for isolated non-cosmological examples) to a 3-dex range in  $M_{\star}$ . The extended mass range also shows that the suppression is the most pronounced in low-mass objects ( $M_{\star} \leq 10^6 M_{\odot}$ ) for which shallow gravitational potential wells increases sensitivity to radiative feedback (Figure 5).

Despite the significant change in outflow behaviours, stellar masses at  $z = 0$  are converged to  $\approx 40\%$  on average across the suite, a shift well within uncertainties (Figure 2). In fact, most scaling relations of dwarf galaxy observables cannot distinguish between two models. The  $M_V$ - $r_{1/2,V}$  relation (Figure 6), the  $M_{\star} - M_{\text{H I}}$  relation (Figure 8) and the  $M_{\star}$ - $(12 + \log(\text{O}/\text{H}))$  relation (Figure 9) all show-case small shifts compared to the width of the observational scatter and its error bars.

Only the  $M_V$ - $([\text{Fe}/\text{H}])$  presents a strong response to our model

changes, with both models tracking the observed slope of the mass-metallicity relation but respectively scattering at the lower and upper end of the observed scatter (Figure 7). Higher  $([\text{Fe}/\text{H}])$  in the new simulations are driven by the combined update to the chemical modelling – yield updates increasing iron production – and the weaker galactic outflows – that increase iron retention in the ISM (Figure 10).

These results confirm the expectation from Agertz et al. (2020) that the  $M_V$ - $([\text{Fe}/\text{H}])$  relation is the most sensitive probe of stellar and ISM physics in dwarf galaxies. There, we used a single dwarf galaxy ran with and without radiative transfer. This paper extends these results to a much wider range of stellar and halo masses, showing that the slope of the  $M_V$ - $([\text{Fe}/\text{H}])$  readily emerges in both models but that the normalization of the relation directly reflects the combination of modelling choices that control iron production (e.g. CCSNe yields) and retention (e.g. outflow strength).

A promising way to distinguish between these two effects will be to leverage the wealth of new chemical data from spectroscopic surveys (e.g.  $> 50,000$  chemical abundances of dwarf galaxy stars with 4MOST; Skúladóttir et al. 2023). Unpicking the relative abundances of each element and their scatter will provide stronger constraints on the chemical yields of stars at low metallicities. In parallel, direct observations of dwarf galaxies’ outflows, their velocities, and their mass-loading factors is now possible thanks to the advancements in IFU technology (e.g. McQuinn et al. 2019; Xu et al. 2022; Marasco et al. 2023). A careful comparison of these emission-line derived observations to simulations like the EDGE2 suite should allow us to constrain the physical mechanisms driving galactic outflows in dwarf galaxies. And new observables, such as the distribution of ionized metal absorbers in the circumgalactic medium of dwarf irregulars (e.g. Zheng et al. 2019, 2020, 2024) inform us on the baryon cycle of dwarf galaxies and offer orthogonal constraints on the accretion-outflow cycle to be explored in the coming years.

The robust emergence of several dwarf galaxy scaling relations and the relative convergence of our results signal that cosmological simulations of dwarf galaxies have entered an era of precision. Even with a committed theoretical variation (the inclusion of a new feedback channel) which changes by order of magnitudes the outflow behaviour of simulated dwarf galaxies, much of their general characteristics remain broadly compatible with observational data. Nonetheless, there remains clear numerical limitations to our simulations. While SN feedback is now well resolved and converged, radiative feedback remains less accurately captured (Section 5). Moreover, other theoretical uncertainties that impact the strength of galactic outflows in dwarf galaxies remain to be quantified, for example the importance of AGN or cosmic rays in this regime. Addressing these challenges will be the focus of future works from the EDGE collaboration. But ultimately, the convergence of basic scaling relations makes for an exciting moment, providing us with a solid foundation to differentiate between these mechanisms and interpret new dwarf galaxy data coming in the next decade.

## ACKNOWLEDGEMENTS

MR thanks Astha Agarwal, Harley Katz, Taysun Kimm, Joakim Rosdahl and Mahsa Sanati for useful discussions and comments during the preparation of this manuscript. MR acknowledges support from the Beecroft Fellowship funded by Adrian Beecroft. ET acknowledges the UKRI Science and Technology Facilities Council (STFC) for support (grant ST/V50712X/1). O.A. acknowledges support from the Knut and Alice Wallenberg Foundation, the Swedish Research Council (grant 2019-04659), the Swedish National Space Agency

(SNSA Dnr 2023-00164), and the LMK foundation. This project has received funding from the European Union's Horizon 2020 research and innovation programme under grant agreement No. 818085 GMGalaxies. This work was performed using the DiRAC Data Intensive service at Leicester, operated by the University of Leicester IT Services, which forms part of the STFC DiRAC HPC Facility ([www.dirac.ac.uk](http://www.dirac.ac.uk)). The equipment was funded by BEIS capital funding via STFC capital grants ST/K000373/1 and ST/R002363/1 and STFC DiRAC Operations grant ST/R001014/1. DiRAC is part of the National e-Infrastructure. The authors acknowledge the use of the UCL Grace High Performance Computing Facility, the Surrey Eureka supercomputer facility, and their associated support services. This work was partially supported by the UCL Cosmoparticle Initiative.

We thank the developers and maintainers of PYNBODY (Pontzen et al. 2013), TANGOS (Pontzen & Tremmel 2018), NUMPY (van der Walt et al. 2011; Harris et al. 2020), SCIPY (Virtanen et al. 2020), JUPYTER (Ragan-Kelley et al. 2014), MATPLOTLIB (Hunter 2007), the Astrophysics Data Service and the arXiv preprint repository for providing open-source softwares that were used extensively in this work.

## DATA AVAILABILITY

The data underlying this article will be shared upon reasonable request to the corresponding author.

## AUTHOR CONTRIBUTIONS

The main roles of the authors were, using the CRediT (Contribution Roles Taxonomy) system<sup>2</sup>:

MR: Conceptualization; Data curation; Formal analysis; Funding acquisition; Investigation; Writing – original draft. ET: Data curation; Investigation; Writing – review and editing. EG: Data curation; Investigation; Writing – review and editing. SK: Data curation; Investigation; Writing – review and editing. EA: Investigation; Methodology; Software; Writing – review and editing. AP: Conceptualization; Funding acquisition; Software; Writing – review and editing. OA: Conceptualization; Methodology; Software; Writing – review and editing. JR: Conceptualization; Project administration; Resources; Writing – review and editing. CC: Methodology; Software; Writing – review and editing. RY: Writing – review and editing. MO: Data Curation; Investigation; Writing – review and editing. DS: Data curation; Writing – review and editing. AS: Conceptualization; Writing – review and editing. JB: Data curation; Writing – review and editing. KQ: Writing – review and editing. CM: Writing – review and editing. PD: Writing – review and editing.

## REFERENCES

- Adams E. A. K., Oosterloo T. A., 2018, *A&A*, 612, A26
- Agertz O., Teyssier R., Moore B., 2011, *MNRAS*, 410, 1391
- Agertz O., Kravtsov A. V., Leitner S. N., Gnedin N. Y., 2013, *ApJ*, 770, 25
- Agertz O., et al., 2020, *MNRAS*, 491, 1656
- Agertz O., et al., 2021, *MNRAS*, 503, 5826
- Andersson E. P., Mac Low M.-M., Agertz O., Renaud F., Li H., 2024, *A&A*, 681, 13
- Andersson E. P., Rey M. P., Pontzen A., Cadiou C., Agertz O., Read J. I., Martín N. F., 2025, *ApJ*, 978, 129
- Anglés-Alcázar D., et al., 2021, *ApJ*, 917, 53
- Arjona-Galvez E., Di Cintio A., Grand R. J. J., 2024, *A&A*, 690, A286
- Asplund M., Grevesse N., Sauval A. J., Scott P., 2009, *ARA&A*, 47, 481
- Aubert D., Teyssier R., 2010, *ApJ*, 724, 244
- Aubert D., Pichon C., Colombi S., 2004, *MNRAS*, 352, 376
- Beckmann R. S., Slyz A., Devriendt J., 2018, *MNRAS*, 478, 995
- Benítez-Llambay A., Frenk C., 2020, *MNRAS*, 498, 4887
- Benítez-Llambay A., Fumagalli M., 2021, *ApJ*, 921, L9
- Benítez-Llambay A., Navarro J. F., Abadi M. G., Gottlöber S., Yepes G., Hoffman Y., Steinmetz M., 2015, *MNRAS*, 450, 4207
- Bennet P., et al., 2022, *ApJ*, 924, 98
- Brauer K., et al., 2025, *ApJ*, 980, 41
- Bressan A., Marigo P., Girardi Léo., Salasnich B., Dal Cero C., Rubele S., Nanni A., 2012, *MNRAS*, 427, 127
- Bruce J., Li T. S., Pace A. B., Heiger M., Song Y.-Y., Simon J. D., 2023, *ApJ*, 950, 167
- Brunker S. W., et al., 2019, *AJ*, 157, 76
- Bruzual G., Charlot S., 2003, *MNRAS*, 344, 1000
- Bullock J. S., Boylan-Kolchin M., 2017, *ARA&A*, 55, 343
- Burke C. J., et al., 2022, *MNRAS*, 516, 2736
- Buttry R., et al., 2022, *MNRAS*, 514, 1706
- Cadiou C., Dubois Y., Pichon C., 2019, *A&A*, 621, A96
- Cadiou C., Pontzen A., Peiris H. V., 2021, *MNRAS*, 502, 5480
- Cameron A. J., Katz H., Rey M. P., 2023, *MNRAS*, 552, L89
- Cerny W., et al., 2023a, *ApJ*, 942, 111
- Cerny W., et al., 2023b, *ApJ*, 953, 1
- Cerny W., et al., 2023c, *ApJL*, 953, L21
- Chabrier G., 2003, *PASP*, 115, 763
- Charles E. J. E., et al., 2023, *MNRAS*, 521, 3527
- Chisholm J., Tremonti C. A., Leitherer C., Chen Y., 2017, *MNRAS*, 469, 4831
- Chiti A., et al., 2021, *Nat Ast*, 5, 392
- Chiti A., Simon J. D., Frebel A., Pace A. B., Ji A. P., Li T. S., 2022, *ApJ*, 939, 41
- Christensen C. R., Davé R., Governato F., Pontzen A., Brooks A., Munshi F., Quinn T., Wadsley J., 2016, *ApJ*, 824, 57
- Cioffi D. F., McKee C. F., Bertschinger E., 1988, *ApJ*, 334, 252
- Cole A. A., Weisz D. R., Dolphin A. E., Skillman E. D., McConnachie A. W., Brooks A. M., Leaman R., 2014, *ApJ*, 795, 54
- Collins M. L. M., Read J. I., 2022, *Nat Ast*, 6, 647
- Collins M. L. M., Tollerud E. J., Rich R. M., Ibata R. A., Martin N. F., Chapman S. C., Gilbert K. M., Preston J., 2020, *MNRAS*, 491, 3496
- Collins M. L. M., et al., 2021, *MNRAS*, 505, 5686
- Collins M. L. M., et al., 2024, *MNRAS*, 528, 2614
- Côté B., et al., 2018, *ApJ*, 855, 99
- Courty S., Alimi J. M., 2004, *A&A*, 416, 875
- Curtis M., Sijacki D., 2015, *MNRAS*, 454, 3445
- Davis F., et al., 2022, *MNRAS*, 511, 4109
- Deng Y., Li H., Kannan R., Smith A., Vogelsberger M., Bryan G. L., 2024a, *MNRAS*, 527, 478
- Deng Y., Li H., Liu B., Kannan R., Smith A., Bryan G. L., 2024b, *A&A*, 691, A231
- Efstathiou G., 1992, *MNRAS*, 256, 43P
- Eisenstein D. J., Hut P., 1998, *ApJ*, 498, 137
- Ejdetjärn T., Agertz O., Östlin G., Rey M. P., Renaud F., 2024, *MNRAS*, 534, 135
- Emerick A., Bryan G. L., Mac Low M.-M., 2018, *ApJ*, 865, L22
- Escala I., et al., 2018, *MNRAS*, 474, 2194
- Faucher-Giguère C.-A., 2020, *MNRAS*, 493, 1614
- Ferland G. J., et al., 2017, *Revista Mexicana de Astronomía y Astrofísica*, 53, 385
- Fitts A., et al., 2017, *MNRAS*, 471, 3547
- Fritz T. K., Carrera R., Battaglia G., Taibi S., 2019, *A&A*, 623, A129
- Genel S., et al., 2019, *ApJ*, 871, 21
- Gnedin N. Y., 2000, *ApJ*, 542, 535
- Gnedin N. Y., Abel T., 2001, *New Astronomy*, 6, 437

<sup>2</sup> <https://authorservices.wiley.com/author-resources/Journal-Authors/open-access/credit.html>



- Goater A., et al., 2024, *MNRAS*, 527, 2403
- Gray E. I., et al., 2024, EDGE: A New Model for Nuclear Star Cluster Formation in Dwarf Galaxies ([arXiv:2405.19286](https://arxiv.org/abs/2405.19286))
- Greif T. H., Glover S. C. O., Bromm V., Klessen R. S., 2010, *ApJ*, 716, 510
- Guillet T., Teyssier R., 2011, *J. Comput. Phys.*, 230, 4756
- Gutcke T. A., Pakmor R., Naab T., Springel V., 2022, *MNRAS*, 513, 1372
- Haardt F., Madau P., 1996, *ApJ*, 461, 20
- Hansen T. T., Simon J. D., Li T. S., Sharkey D., Ji A. P., Thompson I. B., Reggiani H. M., Galarza J. Y., 2024, *ApJ*, 968, 21
- Hargis J. R., et al., 2020, *ApJ*, 888, 31
- Harris C. R., et al., 2020, *Nature*, 585, 357
- Heiger M. E., et al., 2024, *ApJ*, 961, 234
- Herzog G., Benítez-Llambay A., Fumagalli M., 2023, *MNRAS*, 518, 6305
- Hoefl M., Yepes G., Gottlöber S., Springel V., 2006, *MNRAS*, 371, 401
- Homma D., et al., 2019, *PASJ*, 71, 94
- Homma D., et al., 2024, *PASJ*, 76, 733
- Hopkins P. F., et al., 2018, *MNRAS*, 480, 800
- Hopkins P. F., et al., 2022, *MNRAS*, 519, 3154
- Hui L., Gnedin N. Y., 1997, *MNRAS*, 292, 27
- Hunter J. D., 2007, *CiSE*, 9, 90
- Jaacks J., Thompson R., Finkelstein S. L., Bromm V., 2018, *MNRAS*, 475, 4396
- Janesh W., Rhode K. L., Salzer J. J., Janowiecki S., Adams E. A. K., Haynes M. P., Giovanelli R., Cannon J. M., 2019, *AJ*, 157, 183
- Jenkins S. A., Li T. S., Pace A. B., Ji A. P., Kuposov S. E., Mutlu-Pakdil B., 2021, *ApJ*, 920, 92
- Jeon M., Besla G., Bromm V., 2017, *ApJ*, 848, 85
- Jeon M., Bromm V., Besla G., Yoon J., Choi Y., 2021, *MNRAS*, 502, 1
- Ji A. P., Frebel A., Simon J. D., Geha M., 2016a, *ApJ*, 817, 41
- Ji A. P., Frebel A., Simon J. D., Chiti A., 2016b, *ApJ*, 830, 93
- Ji A. P., Frebel A., Ezzeddine R., Casey A. R., 2016c, *ApJ*, 832, L3
- Ji A. P., Simon J. D., Frebel A., Venn K. A., Hansen T. T., 2019, *ApJ*, 870, 83
- Ji A. P., et al., 2020, *ApJ*, 889, 27
- Ji A. P., et al., 2021, *ApJ*, 921, 32
- Jones M. G., et al., 2023, *ApJL*, 957, L5
- Jones M. G., et al., 2024, *ApJL*, 971, L37
- Katz H., et al., 2020, *MNRAS*, 494, 2200
- Katz H., et al., 2023, *Open J. of Astrophysics*, 6, 44
- Katz H., Rey M. P., Cadiou C., Kimm T., Agertz O., 2024, The Impact of Star Formation and Feedback Recipes on the Stellar Mass and Interstellar Medium of High-Redshift Galaxies ([arXiv:2411.07282](https://arxiv.org/abs/2411.07282))
- Keller B. W., Wadsley J. W., Wang L., Kruijssen J. M. D., 2019, *MNRAS*, 482, 2244
- Kennicutt Jr. R. C., 1998, *ApJ*, 498, 541
- Kewley L. J., Ellison S. L., 2008, *ApJ*, 681, 1183
- Kim C.-G., Ostriker E. C., 2015, *ApJ*, 802, 99
- Kim J.-h., et al., 2014, *ApJS*, 210, 14
- Kim S. Y., et al., 2024, EDGE: Predictable Scatter in the Stellar Mass–Halo Mass Relation of Dwarf Galaxies ([arXiv:2408.15214](https://arxiv.org/abs/2408.15214))
- Kimm T., Cen R., Devriendt J., Dubois Y., Slyz A., 2015, *MNRAS*, 451, 2900
- Kirby E. N., Cohen J. G., Guhathakurta P., Cheng L., Bullock J. S., Gallazzi A., 2013, *ApJ*, 779, 102
- Kirby E. N., Bullock J. S., Boylan-Kolchin M., Kaplinghat M., Cohen J. G., 2014, *MNRAS*, 439, 1015
- Kirby E. N., Rizzi L., Held E. V., Cohen J. G., Cole A. A., Manning E. M., Skillman E. D., Weisz D. R., 2017, *ApJ*, 834, 9
- Kirby E. N., Gilbert K. M., Escala I., Wojno J., Guhathakurta P., Majewski S. R., Beaton R. L., 2020, *AJ*, 159, 46
- Koribalski B. S., et al., 2020, *ASS*, 365, 118
- Koudmani S., Henden N. A., Sijacki D., 2021, *MNRAS*, 503, 3568
- Koudmani S., Sijacki D., Smith M. C., 2022, *MNRAS*, 516, 2112
- Kravtsov A., Manwadkar V., 2022, *MNRAS*, 514, 2667
- Kroupa P., 2001, *MNRAS*, 322, 231
- Kvasova K., Kirby E. N., Beaton R. L., 2024, *ApJ*, 972, 180
- LIGO and Virgo Scientific Collaboration et al., 2017, *PRL*, 119, 161101
- Lewis A., Challinor A., Lasenby A., 2000, *ApJ*, 538, 473
- Li T. S., et al., 2017, *ApJ*, 838, 8
- Li T. S., et al., 2018, *ApJ*, 857, 145
- Li J., Greene J. E., Carlsten S. G., Danieli S., 2024, *ApJL*, 975, L23
- Limongi M., Chieffi A., 2018, *ApJS*, 237, 13
- Liu W., Veilleux S., Canalizo G., Rupke D. S. N., Manzano-King C. M., Bohn T., U V., 2020, *ApJ*, 905, 166
- Liu W., et al., 2024, *ApJ*, 965, 152
- Longeard N., et al., 2018, *MNRAS*, 480, 2609
- Maoz D., Mannucci F., Brandt T. D., 2012, *MNRAS*, 426, 3282
- Marasco A., et al., 2023, *A&A*, 670, A92
- Martin-Alvarez S., Sijacki D., Haehnelt M. G., Farcy M., Dubois Y., Belokurov V., Rosdahl J., Lopez-Rodriguez E., 2023, *MNRAS*, 525, 3806
- Martinez-Delgado D., Stein M., Pawlowski M. S., Makarov D., Makarova L., Donatiello G., Lang D., 2024, Tracing Satellite Planes in the Sculptor Group: II. Discovery of Five Faint Dwarf Galaxies in the DESI Legacy Survey ([arXiv:2405.03769](https://arxiv.org/abs/2405.03769))
- Martizzi D., Faucher-Giguère C.-A., Quataert E., 2015, *MNRAS*, 450, 504
- Mau S., et al., 2020, *ApJ*, 890, 136
- McConnachie A. W., 2012, *AJ*, 144, 4
- McConnachie A. W., Venn K. A., 2020, *AJ*, 160, 124
- McConnachie A. W., Higgs C. R., Thomas G. F., Venn K. A., Côté P., Battaglia G., Lewis G. F., 2021, *MNRAS*, 501, 2363
- McNanna M., et al., 2024, *ApJ*, 961, 126
- McQuinn M., 2016, *ARA&A*, 54, 313
- McQuinn K. B. W., et al., 2015, *ApJ*, 812, 158
- McQuinn Kristen. B. W., van Zee L., Skillman E. D., 2019, *ApJ*, 886, 74
- McQuinn Kristen. B. W., et al., 2020, *ApJ*, 891, 181
- McQuinn K. B. W., et al., 2021, *ApJ*, 918, 23
- McQuinn K. B. W., Mao Y.-Y., Buckley M. R., Shih D., Cohen R. E., Dolphin A. E., 2023, *ApJ*, 944, 14
- Mezcua M., Sánchez H. D., 2024, *MNRAS*, 528, 5252
- Mitchell P. D., Schaye J., Bower R. G., Crain R. A., 2020, *MNRAS*, 494, 3971
- Monzon J. S., van den Bosch F. C., Mitra K., 2024, *ApJ*, 976, 197
- Muni C., Pontzen A., Read J. I., Agertz O., Rey M. P., Taylor E., 2025, *MNRAS*, 536, 314
- Munshi F., Brooks A. M., Christensen C., Applebaum E., Holley-Bockelmann K., Quinn T. R., Wadsley J., 2019, *ApJ*, 874, 40
- Munshi F., Brooks A., Applebaum E., Christensen C., Sligh J. P., Quinn T., 2021, *ApJ*, 923, 35
- Muratov A. L., Kereš D., Faucher-Giguère C.-A., Hopkins P. F., Quataert E., Murray N., 2015, *MNRAS*, 454, 2691
- Mutlu-Pakdil B., et al., 2021, *ApJ*, 918, 88
- Naab T., Ostriker J. P., 2017, *ARA&A*, 55, 59
- Nadler E. O., et al., 2020, *ApJ*, 893, 48
- Naiman J. P., et al., 2018, *MNRAS*, 477, 1206
- Nakajima K., et al., 2022, *ApJS*, 262, 3
- Nebrin O., 2023, *RAA*, 7, 90
- Nelson D., et al., 2019, *MNRAS*, 490, 3234
- Nickerson S., Teyssier R., Rosdahl J., 2018, *MNRAS*, 479, 3206
- Noh Y., McQuinn M., 2014, *MNRAS*, 444, 503
- O’Leary J. A., Steinwandel U. P., Moster B. P., Martin N., Naab T., 2023, *MNRAS*, 520, 897
- Ohlin L., Renaud F., Agertz O., 2019, *MNRAS*, 485, 3887
- Okamoto T., Gao L., Theuns T., 2008, *MNRAS*, 390, 920
- Oñorbe J., Hennawi J. F., Lukić Z., 2017, *ApJ*, 837, 106
- Orkney M. D. A., et al., 2021, *MNRAS*, 504, 3509
- Orkney M. D. A., et al., 2022, *MNRAS*, 515, 185
- Orkney M. D. A., Taylor E., Read J. I., Rey M. P., Pontzen A., Agertz O., Kim S. Y., Delorme M., 2023, *MNRAS*, 525, 3516
- Pace A. B., et al., 2020, *MNRAS*, 495, 3022
- Pandya V., et al., 2021, *MNRAS*, 508, 2979
- Pignatari M., et al., 2016, *ApJS*, 225, 24
- Planck Collaboration et al., 2014, *A&A*, 571, A16
- Planck Collaboration et al., 2020, *A&A*, 641, A6
- Pontzen A., Governato F., 2014, *Nature*, 506, 171
- Pontzen A., Tremmel M., 2018, *ApJS*, 237, 23
- Pontzen A., Roškar R., Stinson G., Woods R., 2013, Astrophysics Source Code Library, p. ascl:1305.002

- Pontzen A., Tremmel M., Roth N., Peiris H. V., Saintonge A., Volonteri M., Quinn T., Governato F., 2017, *MNRAS*, 465, 547
- Pontzen A., Rey M. P., Cadiou C., Agertz O., Teyssier R., Read J., Orkney M. D. A., 2021, *MNRAS*, 501, 1755
- Power C., Navarro J. F., Jenkins A., Frenk C. S., White S. D. M., Springel V., Stadel J., Quinn T., 2003, *MNRAS*, 338, 14
- Prgomet M., Rey M. P., Andersson E. P., Segovia Otero A., Agertz O., Renaud F., Pontzen A., Read J. I., 2022, *MNRAS*, 513, 2326
- Ragan-Kelley M., Perez F., Granger B., Kluyver T., Ivanov P., Frederic J., Bussonnier M., 2014, American Geophysical Union, 2014, H44D
- Raiteri C. M., Villata M., Navarro J. F., 1996, *Astronomy and Astrophysics*, v.315, p.105-115, 315, 105
- Rasera Y., Teyssier R., 2006, *A&A*, 445, 1
- Read J. I., Iorio G., Agertz O., Fraternali F., 2017, *MNRAS*, 467, 2019
- Reines A. E., Greene J. E., Geha M., 2013, *ApJ*, 775, 116
- Reines A. E., Condon J. J., Darling J., Greene J. E., 2020, *ApJ*, 888, 36
- Revaz Y., Jablonka P., 2018, *A&A*, 616, A96
- Rey M. P., Pontzen A., 2018, *MNRAS*, 474, 45
- Rey M. P., Pontzen A., Saintonge A., 2019a, *MNRAS*, 485, 1906
- Rey M. P., Pontzen A., Agertz O., Orkney M. D. A., Read J. I., Saintonge A., Pedersen C., 2019b, *ApJL*, 886, L3
- Rey M. P., Pontzen A., Agertz O., Orkney M. D. A., Read J. I., Rosdahl J., 2020, *MNRAS*, 497, 1508
- Rey M. P., Pontzen A., Agertz O., Orkney M. D. A., Read J. I., Saintonge A., Kim S. Y., Das P., 2022, *MNRAS*, 511, 5672
- Rey M. P., Katz H. B., Cameron A. J., Devriendt J., Slyz A., 2024a, *MNRAS*, 528, 5412
- Rey M. P., et al., 2024b, *MNRAS*, 529, 2379
- Richstein H., et al., 2022, *ApJ*, 933, 217
- Ritter C., Herwig F., Jones S., Pignatari M., Fryer C., Hirschi R., 2018, *MNRAS*, 480, 538
- Rosdahl J., Blaizot J., 2012, *MNRAS*, 423, 344
- Rosdahl J., Teyssier R., 2015, *MNRAS*, 449, 4380
- Rosdahl J., Blaizot J., Aubert D., Stranex T., Teyssier R., 2013, *MNRAS*, 436, 2188
- Rosdahl J., et al., 2018, *MNRAS*
- Rosen A., Bregman J. N., 1995, *ApJ*, 440, 634
- Roth N., Pontzen A., Peiris H. V., 2016, *MNRAS*, 455, 974
- Sales L. V., Wetzel A., Fattahi A., 2022, *Nat Ast*, 6, 897
- Sanati M., Jeanquartier F., Revaz Y., Jablonka P., 2023, *A&A*, 669, A94
- Sand D. J., Spekkens K., Crnojević D., Hargis J. R., Willman B., Strader J., Grillmair C. J., 2015, *ApJL*, 812, L13
- Sand D. J., et al., 2022, *ApJL*, 935, L17
- Schmidt M., 1959, *ApJ*, 129, 243
- Scholte D., et al., 2025, *MNRAS*, 535, 2341
- Seitzzahl I. R., et al., 2013, *MNRAS*, 429, 1156
- Sharma R. S., Brooks A. M., Tremmel M., Bellvary J., Quinn T. R., 2023, *ApJ*, 957, 16
- Simon J. D., 2018, *ApJ*, 863, 89
- Simon J. D., 2019, *ARA&A*, 57, 375
- Simon J. D., et al., 2023, *ApJ*, 944, 43
- Skúladóttir Á., et al., 2023, *The Messenger*, 190, 19
- Smith M. C., 2021, *MNRAS*, 502, 5417
- Smith B. D., et al., 2017, *MNRAS*, 466, 2217
- Smith M. C., Bryan G. L., Somerville R. S., Hu C.-Y., Teyssier R., Burkhardt B., Hernquist L., 2021, *MNRAS*, 506, 3882
- Smith S. E. T., et al., 2023, *AJ*, 166, 76
- Smith S. E. T., et al., 2024, *ApJ*, 961, 92
- Snaith O. N., Park C., Kim J., Rosdahl J., 2018, *MNRAS*, 477, 983
- Stanway E. R., Eldridge J. J., Becker G. D., 2016, *MNRAS*, 456, 485
- Stopyra S., Pontzen A., Peiris H., Roth N., Rey M. P., 2021a, *ApJS*, 252, 28
- Stopyra S., Peiris H. V., Pontzen A., 2021b, *MNRAS*, 500, 4173
- Strömgren B., 1939, *ApJ*, 89, 526
- Taibi S., Battaglia G., Rejkuba M., Leaman R., Kacharov N., Iorio G., Jablonka P., Zoccali M., 2020, *A&A*, 635, A152
- Tan C. Y., et al., 2025, *ApJ*, 979, 176
- Tarumi Y., Yoshida N., Frebel A., 2021, *ApJL*, 914
- Teyssier R., 2002, *A&A*, 385, 337
- Thielemann F. K., Nomoto K., Yokoi K., 1986, *Astronomy and Astrophysics*, 158, 17
- Thornton K., Gaudlitz M., Janka H. T., Steinmetz M., 1998, *ApJ*, 500, 95
- Tollet E., et al., 2016, *MNRAS*, 456, 3542
- Toro E. F., Spruce M., Speares W., 1994, *Shock Waves*, 4, 25
- Torrealba G., Kopysov S. E., Belokurov V., Irwin M., 2016, *MNRAS*, 459, 2370
- Torrealba G., et al., 2018, *MNRAS*, 475, 5085
- Torrealba G., et al., 2019, *MNRAS*, 488, 2743
- Tweed D., Devriendt J., Blaizot J., Colombi S., Slyz A., 2009, *A&A*, 506, 647
- Virtanen P., et al., 2020, *Nat Methods*, 17, 261
- Visbal E., Bryan G. L., Haiman Z., 2020, *ApJ*, 897, 95
- Wang L., Dutton A. A., Stinson G. S., Macciò A. V., Penzo C., Kang X., Keller B. W., Wadsley J., 2015, *MNRAS*, 454, 83
- Wang Y., Nadler E. O., Mao Y.-Y., Adhikari S., Wechsler R. H., Behroozi P., 2021, *ApJ*, 915, 116
- Wasleske E. J., Baldassare V. F., 2024, *ApJ*, 971, 68
- Wheeler C., et al., 2019, *MNRAS*, 490, 4447
- Wojno J., Gilbert K. M., Kirby E. N., Escala I., Beaton R. L., Tollerud E. J., Majewski S. R., Guhathakurta P., 2020, *ApJ*, 895, 78
- Woolsey S. E., Heger A., 2007, *Physics Reports*, 442, 269
- Wright A. C., Brooks A. M., Weisz D. R., Christensen C. R., 2019, *MNRAS*, 482, 1176
- Xu Y., et al., 2022, *ApJ*, 929, 134
- Xu J.-L., Zhu M., Yu N., Zhang C.-P., Liu X.-L., Ai M., Jiang P., 2023, *ApJL*, 944, L40
- Yates R. M., Schady P., Chen T.-W., Schweyer T., Wiseman P., 2020, *A&A*, 634, A107
- Zel'dovich Ya. B., 1970, *A&A*, 5, 84
- Zheng Y., et al., 2019, *MNRAS*, 490, 467
- Zheng Y., Emerick A., Putman M. E., Werk J. K., Kirby E. N., Peek J. E. G., 2020, *ApJ*, 2020, 133
- Zheng Y., et al., 2024, *ApJ*, 960, 21
- van Cappellen W. A., et al., 2022, *A&A*, 658, A146
- van der Walt S., Colbert S. C., Varoquaux G., 2011, *CiSe*, 13, 22

## APPENDIX A: SUMMARY OF EDGE1 AND EDGE2 PROPERTIES

Table A1 summarizes the properties of the simulated dwarf galaxies with the EDGE1 and EDGE2 models at  $z = 0$ .

## APPENDIX B: RESOLVED FEEDBACK IN EDGE2 SIMULATIONS

The strength of the EDGE approach lies in its uncompromisingly high resolution to directly resolve key stellar feedback processes in the ISM of our dwarf galaxies. We quantify this statement in this Appendix.

### B1 SN feedback

Resolving the cooling radius of SNe remnants is a key modelling milestone to accurately capture the momentum-build up during the Sedov-Taylor phase (e.g. Kim & Ostriker 2015). Our injection scheme computes the cooling radius as

$$R_{\text{cool}} = 30.0 \text{ pc} \left( \frac{n_{\text{H}}}{\text{cm}^{-3}} \right)^{-3/7} \left( \frac{E}{10^{51} \text{ erg}} \right)^{2/7} \left( \frac{Z}{Z_{\odot}} + 0.01 \right)^{1/7}, \quad (\text{B1})$$

where  $n_{\text{H}}$  is the hydrogen density in the gas cell,  $E$  is the total energy injected (this can be  $\geq 10^{51}$  erg if more than one SN are exploding in the same timestep), and  $Z$  is the gas metallicity (see Hopkins

**Table A1.** Properties of simulated dwarf galaxies with the EDGE1 and EDGE2 models (E1 and E2 columns, respectively) at  $z = 0$  (see Section 4 for details on how each property is computed). Haloes with only an EDGE2 column are new initial conditions that do not have an EDGE1 counterpart (see Section 2.1). Two haloes were stopped at higher redshifts due to their computational cost (see Section 3.1) – their properties are indicated at the labelled redshift.

Object	$M_{200}$ ( $M_{\odot}$ )	$M_{\star}$ ( $M_{\odot}$ )		$M_V$		$r_{1/2,V}$ (kpc)		$M_{H_I}$ ( $M_{\odot}$ )		$\langle [Fe/H] \rangle$		$\langle 12 + \log(O/H) \rangle$	
		E1	E2	E1	E2	E1	E2	E1	E2	E1	E2	E1	E2
Halo 1445	$1.2 \times 10^9$	$7.9 \times 10^4$	$5.8 \times 10^4$	-6.35	-5.36	0.20	0.29	$1.2 \times 10^1$	$4.9 \times 10^1$	-2.58	-2.24	6.31	7.25
Halo 1459: GM earlier	$1.4 \times 10^9$	$4.9 \times 10^5$	$4.4 \times 10^5$	-8.29	-7.50	0.16	0.22	$1.3 \times 10^1$	$4.3 \times 10^1$	-2.34	-1.78	6.63	8.39
Halo 1459	$1.4 \times 10^9$	$2.6 \times 10^5$	$3.6 \times 10^5$	-7.62	-7.29	0.23	0.25	$1.9 \times 10^1$	$4.9 \times 10^1$	-2.40	-2.04	6.73	8.04
Halo 1459: GM later	$1.4 \times 10^9$	$1.2 \times 10^5$	$7.5 \times 10^4$	-6.84	-5.60	0.31	0.28	$1.7 \times 10^1$	$7.4 \times 10^1$	-2.58	-2.03	6.55	7.25
Halo 1459: GM latest	$1.4 \times 10^9$	$4.5 \times 10^4$	$1.5 \times 10^4$	-5.72	-3.94	1.00	2.63	$2.0 \times 10^1$	$1.0 \times 10^2$	-2.93	-2.53	6.44	6.35
Halo 600	$3.4 \times 10^9$	$5.1 \times 10^5$	$6.2 \times 10^5$	-8.77	-9.83	0.23	0.30	$5.7 \times 10^5$	$1.8 \times 10^6$	-2.43	-1.49	7.35	7.37
Halo 600: GM later	$3.2 \times 10^9$	$3.9 \times 10^5$	$6.4 \times 10^4$	-8.18	-7.00	0.38	0.10	$2.1 \times 10^5$	$3.9 \times 10^5$	-2.50	-2.70	6.64	6.80
Halo 605	$3.3 \times 10^9$	$1.7 \times 10^6$	$2.9 \times 10^6$	-9.73	-9.91	0.26	0.32	$3.2 \times 10^5$	$7.5 \times 10^5$	-2.21	-1.35	7.30	7.73
Halo 624	$2.5 \times 10^9$	$5.9 \times 10^5$	$4.5 \times 10^5$	-8.93	-8.12	0.38	0.63	$2.3 \times 10^5$	$3.1 \times 10^5$	-2.30	-1.98	6.68	7.27
Halo 624: GM higher mass	$3.8 \times 10^9$	$1.5 \times 10^6$	$1.9 \times 10^6$	-9.63	-9.83	0.31	0.25	$2.3 \times 10^5$	$1.6 \times 10^6$	-2.17	-1.60	7.42	7.50
Halo 383: GM earlier	$5.8 \times 10^9$	$4.4 \times 10^6$	$2.1 \times 10^7$	-10.88	-12.19	0.33	0.49	$3.8 \times 10^5$	$3.6 \times 10^6$	-1.99	-0.96	7.70	8.03
Halo 383	$5.7 \times 10^9$	$3.2 \times 10^6$	$9.4 \times 10^6$	-10.49	-11.85	0.42	0.57	$5.8 \times 10^2$	$7.7 \times 10^6$	-2.02	-1.10	7.10	7.74
Halo 383: stochastic	$5.9 \times 10^9$	$9.6 \times 10^6$	$1.1 \times 10^7$	-11.76	-12.23	0.17	0.35	$5.5 \times 10^1$	$4.5 \times 10^6$	-1.87	-1.05	7.38	7.84
Halo 383: GM later	$5.8 \times 10^9$	$3.3 \times 10^6$	$3.9 \times 10^6$	-10.85	-11.53	0.06	0.78	$5.9 \times 10^2$	$1.8 \times 10^5$	-2.07	-1.26	7.78	7.38
Halo 383: GM higher mass ( $z = 0.9$ )	$7.5 \times 10^9$	$1.1 \times 10^7$	$7.4 \times 10^7$	-12.45	-14.00	0.81	0.55	$7.8 \times 10^6$	$3.5 \times 10^7$	-1.68	-1.60	7.57	7.12
Halo 339	$5.2 \times 10^9$	–	$5.8 \times 10^6$	–	-11.10	–	0.56	–	$3.5 \times 10^6$	–	-1.05	–	7.83
Halo 261: GM earlier	$6.9 \times 10^9$	–	$1.9 \times 10^7$	–	-12.40	–	0.37	–	$5.1 \times 10^6$	–	-1.02	–	7.90
Halo 261	$6.6 \times 10^9$	–	$1.5 \times 10^7$	–	-12.20	–	0.51	–	$7.5 \times 10^6$	–	-1.06	–	7.82
Halo 261: GM later	$6.6 \times 10^9$	–	$9.7 \times 10^6$	–	-12.65	–	0.46	–	$1.5 \times 10^7$	–	-1.15	–	7.59
Halo 153 ( $z=0.6$ )	$1.1 \times 10^{10}$	–	$4.2 \times 10^7$	–	-14.69	–	0.56	–	$4.3 \times 10^7$	–	-1.02	–	7.89

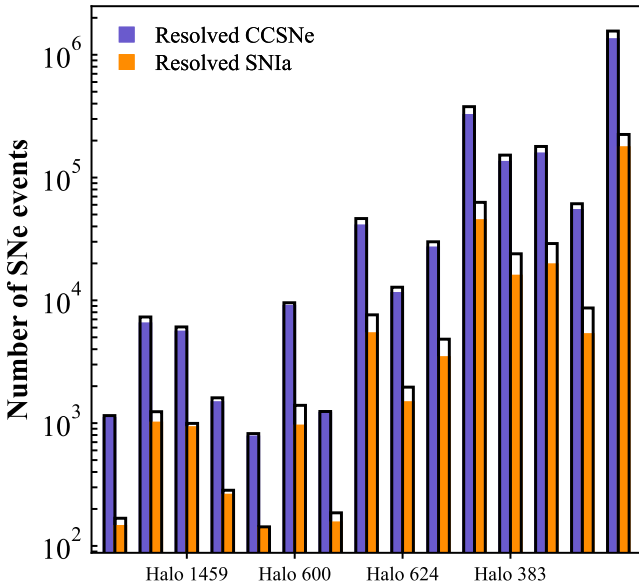


**Figure B1.** Fractions of resolved CCSNe (purple) and SNIa (orange) explosions over the full cosmological history of each galaxy. Bars show the total number of SNe, with filling highlighting those for which we resolve the cooling radius (see text). Each bar pair correspond to an individual dwarf galaxy, ordered with growing halo mass as in Table A1. Irrespective of the mass scale,  $\geq 85\%$  of CCSNe, which dominate the SN feedback budget, are resolved.

et al. 2018, app. D for a derivation of this equation and e.g. Cioffi et al. 1988; Thornton et al. 1998; Kim & Ostriker 2015 for similar scalings).

Figure B1 shows the total number of SNe events in each simulated dwarf galaxy over their whole evolution (bar pair), divided between CCSNe (purple) and SNIa (orange). The filling of the bar indicates

‘resolved’ events where  $R_{\text{cool}} \geq 6 \Delta x$  for which we directly inject thermal energy rather than momentum.

All dwarf galaxies have more than  $\geq 87\%$  of CCSNe events resolved, even as galaxy masses and ISM pressures increase (towards the right). A larger fraction of SNIa are unresolved, most likely because these events can occur in lower-density environments, long after star formation when the adaptive resolution has been degraded. Nonetheless, since CCSNe provide the overwhelming majority of the SN feedback budget, such statistics represent a significant achievement in the robustness of SN feedback modelling.

## B2 Radiative feedback

Even if SN feedback is accurately captured as we have shown above, the coupling of this feedback with the surrounding ISM and the subsequent ability to drive galactic outflows depend on the gas conditions in which the explosions occur. These conditions in turn depend on other, pre-SN feedback channels, especially radiative feedback.

For radiative feedback, the key length scale to resolve is the Ström-gren radius associated to the H II region around the star formation event. Requiring equilibrium between ionization and recombination of a hydrogen sphere, we obtain the Ström-gren radius (Ström-gren 1939) as

$$R_S = \left( \frac{3Q}{4\pi n_H^2 \alpha_B} \right)^{1/3}. \quad (\text{B2})$$

Here  $Q$  is the production rate of hydrogen-ionizing (Lyman-Compton) photons and  $\alpha_B$  is the case-B recombination rate of hydrogen. Note that this equation assumes spherical symmetry, a homogeneous gas distribution and neglects the respective contributions of helium and metallic ions to the ionization and recombination balance. Nonetheless, this is enough to gain order-of-magnitude estimates of whether ionization fronts from photo-ionization feedback are resolved, since gas density is the strongest driver in Equation B2.

We can start by estimating an order of magnitude for  $R_S$  when our star-formation algorithm spawns a stellar particle (see Section 2.4 for details). The density at which stellar particles are spawned peaks around  $\approx 500 m_p \text{ cm}^{-3}$ . Accounting for the depletion of  $300 M_\odot$  into a stellar particle, and assuming a primordial mixture, we input  $n_H = 200 \text{ cm}^{-3}$  into Equation B2. Given our choice of SED (Bruzual & Charlot 2003), a zero-age  $300 M_\odot$  stellar population has an ionizing rate of  $Q \approx 10^{49} \text{ s}^{-1}$  (see e.g. Rosdahl et al. 2018, appendix D for a visualisation). Assuming the temperature-dependent  $\alpha_B$  from Hui & Gnedin (1997) evaluated at  $T = 2 \times 10^4 \text{ K}$  (see their appendix A), we obtain  $R_S \approx 2 \text{ pc}$ . This is already comparable to the maximum resolution of the simulation,  $\Delta x \approx 3 \text{ pc}$ . Pushing to  $n_H = 10^3 \text{ cm}^{-3}$  which is common for star formation events in our simulations, we find  $R_S \approx 0.7 \text{ pc}$ .

The choice of the SED (through  $Q$ ), of the recombination rate ( $\alpha_B$ ) or the assumptions of a primordial plasma will slightly modify these findings, but all these parameters enter Equation B2 with weaker scalings than density. As a result, the Strömgen sphere associated to the birth of a stellar particle is likely to be poorly resolved. This shortcoming is intrinsic to our star formation algorithm and cannot be avoided without modifying the very nature of the recipe (see e.g. Katz et al. 2024 for such a change).

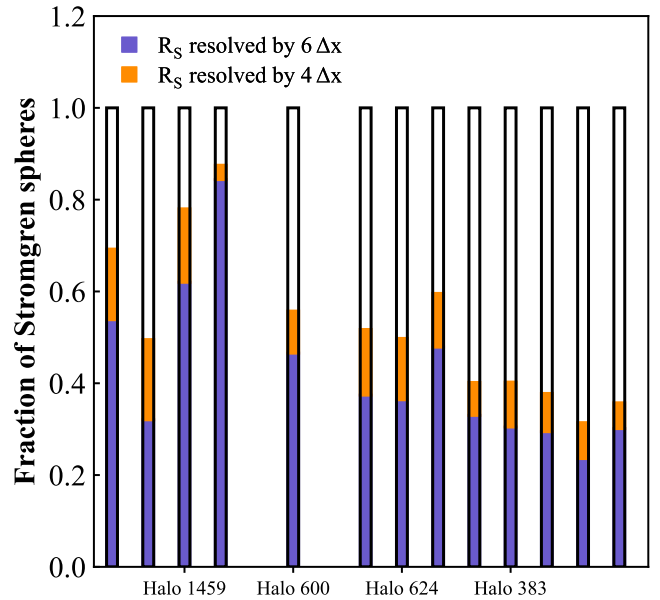
Nonetheless, even if the Strömgen sphere is unresolved at birth, the dynamics of the surrounding ISM could quickly alleviate this issue. Lowering the density to  $n_H = 10 \text{ cm}^{-3}$ , for example, gives  $R_S \approx 14 \text{ pc}$  and a much better-resolved H II region. To test this, we identify young stellar particles with ages  $\leq 5 \text{ Myr}$  for each saved snapshot in the history of our individual galaxies. For each young stellar particle, we identify the density of their host gas cell and their ionizing output using our assumed SED at the particle’s stellar age and metallicity. We then use Equation B2 to compute  $R_S$  (using the same  $\alpha_B$  as previously) and consider a Strömgen sphere to be resolved if  $R_S \geq 6 \Delta x$ . In this case, a spherical H II region would be captured by  $> 200$  resolution elements, which is enough to accurately capture its ionization and temperature structure (e.g. Deng et al. 2024a). We also compute the fraction of resolved Strömgen spheres with  $R_S \geq 4 \Delta x$ , which is a more marginal case with  $\approx 60$  resolution elements per sphere.

Figure B2 show the obtained statistics, with bars showing the resolved fraction of Strömgen spheres over the history of our dwarfs. Some galaxies are missing from the plot as their (short) formation histories and snapshot spacing does not allow sampling of  $< 5 \text{ Myr}$  stars. Across the whole suite, we resolve very well 42% of Strömgen spheres on average, with the smallest fraction being 23% for ‘Halo 383: GM early’. Assuming a less stringent requirement of  $R_S \geq 4 \Delta x$ ; this average fraction climb to 52% with a minimum of 31%. Similarly, shifting the age cut for ‘young’ stars from 5 to 10 Myr leads to a 57% average resolved fraction with a minimum 40% fraction.

Overall, unlike the situation for SNe for which the feedback modelling is nearly all resolved (Figure B1), only a rough half of radiative feedback events are numerically well captured at our resolution. Furthermore, the fraction of resolved events falls rapidly as galaxies become more massive and their ISM denser. This is a clear area of improvement for radiation-hydrodynamics simulations aiming to explicitly model radiative feedback (see Section 5.2 for a discussion).

## APPENDIX C: STAR-FORMATION AND SUPERNOVA STATISTICS

To visualize the consequences of the much denser ISM of the EDGE2 model highlighted in Section 3, Figure C1 shows the densities at



**Figure B2.** Fractions of resolved Strömgen spheres for each dwarf galaxy along the cosmological history of each dwarf, with filling highlighting those for which we resolve the Strömgen radius with 6 (blue) and 4 (orange) resolution elements ( $>200$  and  $60$  elements per sphere, respectively). On average,  $\approx 40\%$  of Strömgen spheres are resolved by  $6\Delta x$  across the suite, with fractions as low as  $\approx 20\%$  for the most massive dwarf galaxies (towards the right). Two dwarf galaxies are absent as their saved snapshots do not sample young stars and H II regions.

which stellar particles are formed (left), and at which the CCSNe from a stellar particle explode (i.e. SNe younger than  $8 \text{ Myr}$  which corresponds to the main sequence lifetime of a  $\approx 20 M_\odot$  massive star). We show the histograms of all SF and SNe events across 4 EDGE2 galaxies that span the full range of  $M_\star$ . (We verified that conclusions are unchanged if using other galaxies.) Unfortunately, star formation and SNe statistics were not recorded in the EDGE1 model, so a direct comparison is not possible.

As expected, no star formation event (left) occurs below our density threshold for SF ( $\geq 300 m_p \text{ cm}^{-3}$ ). For low- $M_\star$  objects (black and brown), there is a clear peak around  $\approx 10^3 m_p \text{ cm}^{-3}$  that quickly tapers off. As dwarfs galaxies increase in  $M_\star$  (green, purple), however, the tail of star-forming events extends to higher densities reaching ( $\geq 10^6 m_p \text{ cm}^{-3}$ ).

The direct consequence is that SNe explosions occur in increasingly dense gas (right panel). The amount of momentum emerging from the Sedov-Taylor phase of a SNe remnant only weakly depends on the background density (e.g. Kim & Ostriker 2015). But since our spatial scales are ultimately limited by numerical resolution, explosions in an increasing dense medium couple this momentum to an ever-increasing mass, thus yielding smaller velocities and weaker outflows<sup>3</sup>.

Part of these effects are driven by our algorithms, which we illustrate now. In particular, our star formation algorithm requires gas to be both sufficiently dense and sufficiently cold to trigger star formation (Section 2.4). Figure C2 shows the same statistics as Figure C1

<sup>3</sup> For a typical Sedov-Taylor momentum ( $p_{SN} = 5 \times 10^5 M_\odot \text{ km s}^{-1}$ ) exploding in a  $3 \text{ pc}$ -cell with  $\rho = 10^5 m_p \text{ cm}^{-3}$ , the generated velocity is  $7 \text{ km s}^{-1}$ . This is insufficient to escape the gravitational potential well of even our small dwarfs ( $v_{\text{circ}} \geq 10 \text{ km s}^{-1}$ ).



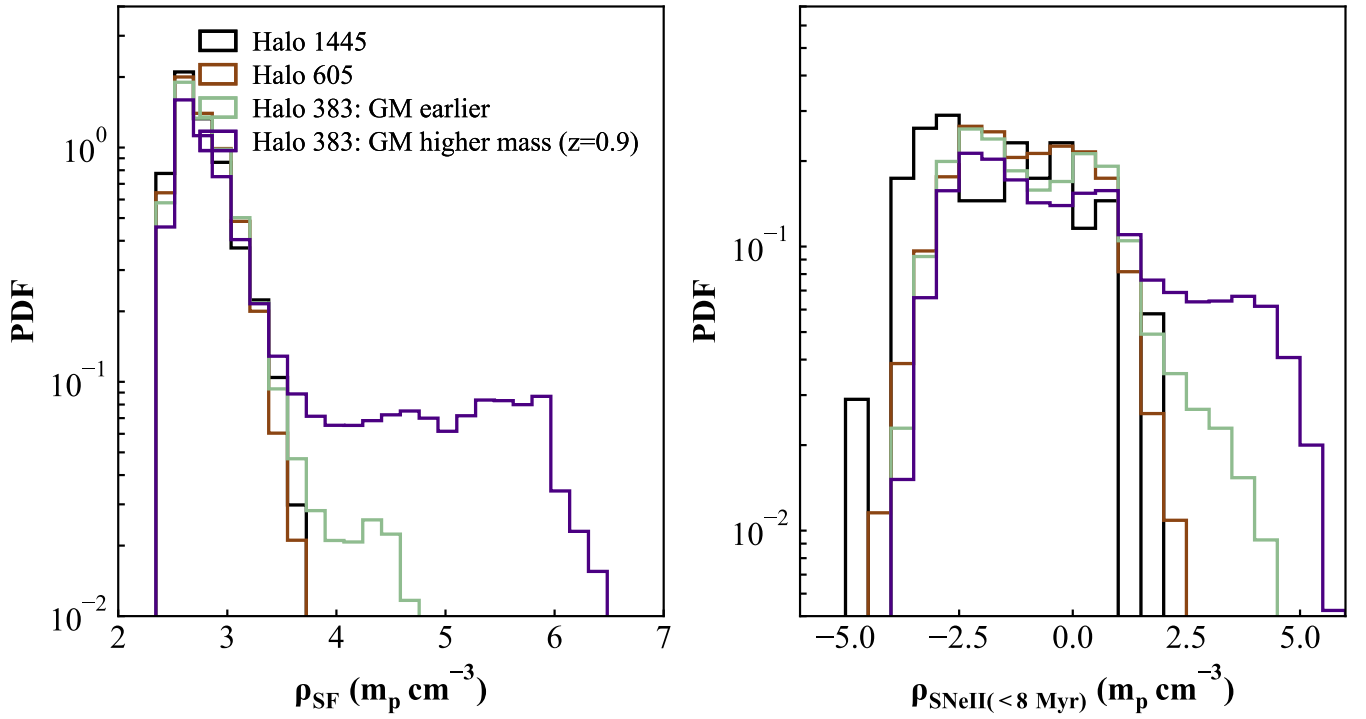


**Figure C1.** Density distribution of star-formation (left) and SNe (right) events across the history of four EDGE2 dwarf galaxies. As objects become more massive, star formation and supernova events at increasingly high densities start to appear.

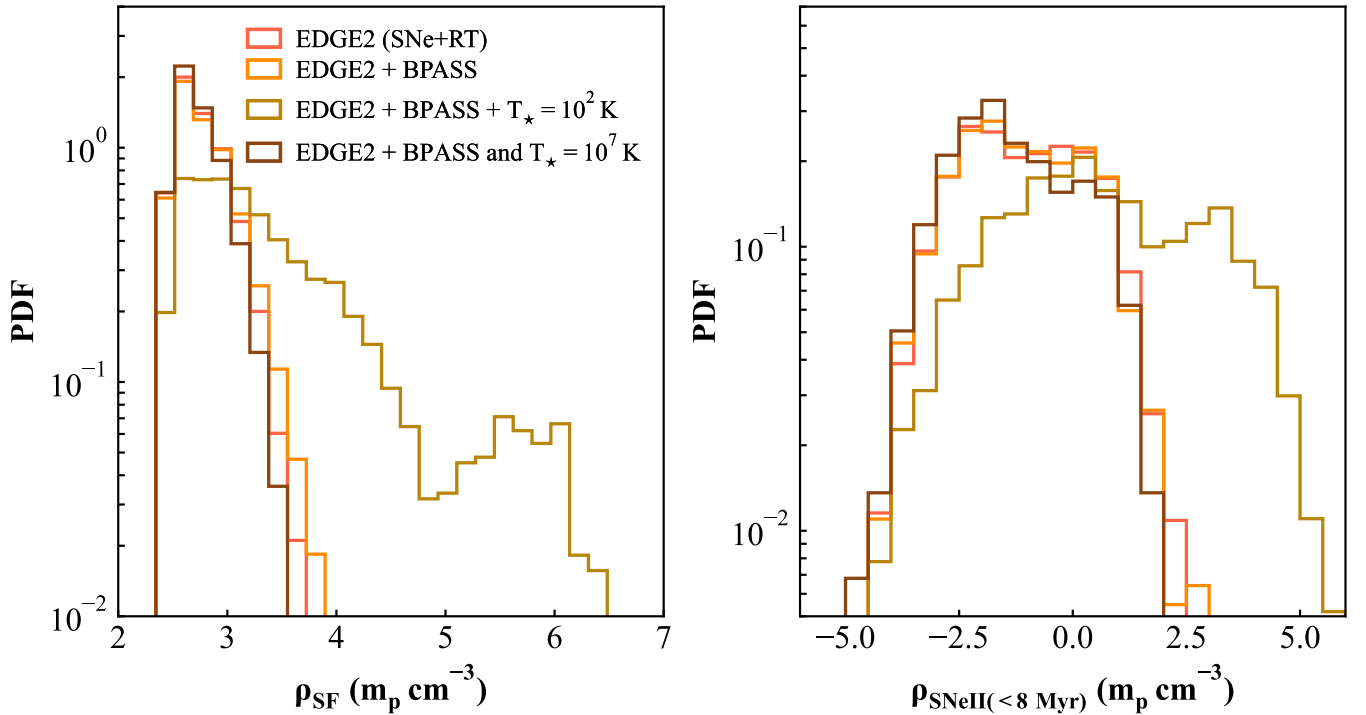


**Figure C2.** Same as Figure C1, but for the four re-simulations of ‘Halo 605’ that vary input parameters as described in Section 5. For the same galaxy, forbidding star formation in warm gas ( $T_{\star} = 10^2$  K, gold) recreates a tail of high-density star formation events by reducing the clustering of star formation and subsequent SN feedback.

for the runs described in Section 5, in which the temperature criteria are raised and lowered. In particular, for a fixed object, a lower  $T_\star$  drives an extended tail of star formation events and SNe at high densities (gold), while a higher  $T_\star$  truncates both to lower densities.

These results should be attributed to interactions between radiative feedback and our star formation prescription. Following a star formation event, the dense gas surrounding the newborn stellar particle is immediately heated to  $T \geq T_\star = 10^3$  K by radiative feedback. Any gas in the immediate vicinity of a star-forming event is thus prevented from forming new stars, staying warm and dense until the first SNe can clear it ( $\approx 5$  Myr later). This suppresses the clustering of star formation and SNe, making it harder to generate powerful outflows.

Even though we isolated the  $T_\star$  parameter here, we stress that this parameter is not the only driver of this behaviour. Rather, the combination of  $T_\star$ , the heating power of stellar radiation, and the surrounding ISM densities driving gas cooling and collapse all contribute towards setting the distribution of star-forming densities. For example, a harder SED will raise more gas over a fixed  $T_\star$  and drive a slightly longer tail of star formation at higher densities (Figure C2, orange versus red). And, at fixed SED and  $T_\star$ , a more massive galaxy with a deeper gravitational potential well and higher ISM densities will retain high densities more effectively and compound this effect (Figure C1, purple versus brown).

Combined with under-resolved radiative feedback events (Appendix B), these findings highlight some key uncertainties remaining in our radiation-hydrodynamics simulations. Nonetheless, while these effects drive large changes on the statistics of star formation and SNe events, they have a much more moderate impact on the integrated  $M_\star$  and other observables (Section 4 and Section 5). Observables such as rest-frame optical emission lines are likely more sensitive to changes in the structure of the ISM and its star-forming regions. In future iterations of the EDGE model, we will continue to improve our implementations and compare with these vital observational clues.

This paper has been typeset from a  $\text{\TeX}/\text{\LaTeX}$  file prepared by the author.